Available online at www.sciencedirect.com
SCIENCE DIRECT®
Journal of Sound and Vibration 294 (2006) 177–204
JOURNAL OF SOUND AND VIBRATION
www.elsevier.com/locate/jsvi

Wall pressure fluctuations induced by turbulent boundary layers over surface discontinuities

R. Camussi[a,*], G. Guj[a], A. Ragni[b]

[a] *Università 'Roma Tre', DIMI, Via della Vasca Navale 79, 00146 Roma, Italy*
[b] *CIRA, Italian Aerospace Research Center, Via Maiorise 1, 81043 Capua (CE), Italy*

Received 21 January 2005; received in revised form 18 October 2005; accepted 4 November 2005
Available online 24 January 2006

Abstract

An experimental investigation of wall pressure fluctuations generated by turbulent boundary layers over surface irregularities has been conducted in a backward–forward-facing step geometry simulating a large aspect-ratio cavity. This simplified incompressible flow model was designed to reproduce geometrical discontinuities present, for example on an aircraft fuselage, and responsible for interior noise generation. This study considers the effects of the main dimensionless parameters, such as the Reynolds number, the normalized incoming boundary layer thickness and its space averaged turbulence intensity, on the Sound Pressure Levels (SPL) and auto-spectra frequency estimates at the wall. Phase averaged temporal quantities are obtained by the application of a wavelet based auto-conditioning method and by velocity/pressure conditional statistics and cross-correlations. This analysis clarifies some relevant properties of the wall pressure fluctuations in the two-steps configuration. Satisfactory scaling for both the SPL and the frequency spectra by dimensionless parameters are obtained and empirical correlations which might be useful for predicting wall pressure properties in practical applications are derived.

1. Introduction

Steps and geometrical irregularities on the exterior surface of modern high-speed passengers aircraft appear, for instance, at skin lap joints or window gaskets and are recognized as potential sources of aerodynamically generated noise. The unsteady aerodynamic pressure field of the surrounding flow induces skin panel vibrations and thus contributes to the interior noise. This effect is known to be relevant especially to the forward airplane fuselage section (see e.g. Ref. [1]). Similar aeroacoustic problems are encountered in other fields of engineering interest, for example, in vehicle or train aerodynamics. In addition to the interior noise generation, wall pressure fluctuations induce skin panel vibration that might affect significantly the fatigue life of the structures causing unpredictable structural damages.

The importance of this subject in practical and basic research applications stimulated many researches in the last decades, most of them aimed at the spatio-temporal characterization of wall pressure fluctuations, which

*Corresponding author. Tel.: +390 6 5517 3291; fax: +390 6 5517 3252.
E-mail address: camussi@uniroma3.it (R. Camussi).

0022-460X/$ - see front matter © 2005 Elsevier Ltd. All rights reserved.
doi:10.1016/j.jsv.2005.11.007

represent the basic quantities to be analyzed to develop predictive or control methods for boundary layers noise. As pointed out in the review paper by Bull [2], the studies conducted so far mainly pertained with the case of turbulent boundary layers (TBL) in equilibrium, developing over smooth surfaces with no flow separation. In regions where surface geometrical discontinuities are located, wall pressure fluctuations and the aerodynamically generated noise are significant, due to the presence of flow separations, recirculations and reattachments. As suggested in Ref. [3], these processes lead to the generation of pressure fluctuations which might be significantly larger than those observed in equilibrium TBL with no separation. Early studies evidenced this phenomenon, for example, in the case of the interior noise generation [4,5] and in the separated flow region downstream a thin fence perpendicular to the incoming flow (see Ref. [6] and the recent experiments in Ref. [7]).

In the present work, the surface irregularities are modelled as large aspect ratio cavities, constituted by a backward-facing step followed by a forward facing step with a streamwise separation much larger than the two steps height and overflown by incompressible TBLs. This geometry has been poorly studied so far even if it appears as a useful simplification for reproducing geometrical irregularities, (such as a window gasket), and for analyzing the aeroacoustics at the wall with a limited number of geometrical parameters. Indeed, a large body of literature is devoted to cavities but having spanwise and streamwise aspect ratios of the order of unity (e.g. Ref. [8]), where the aspect ratio (AR) is defined as the ratio between the steps streamwise separation L or spanwise separation B and the steps height H. In those cases the aerodynamic behavior is three-dimensional and the acoustic properties are strongly influenced by resonance effects and wake reflections (see e.g. the recent review given by Grace [9], and the work in Ref. [10]). The aeroacoustic behavior expected in the geometry presently analyzed is instead quite different with respect to more conventional cavities in view of the large AR which are considered. In the present geometry, the spanwise AR, B/H is larger than 10. This represents the limit indicated in Ref. [11] to consider statistically the two-dimensional centerline flow. The streamwise AR, L/H, is also larger than 10 in order for geometrical similarity to be attained with respect to a typical real window gasket geometry.

In view of the large L/H ratio presently considered, it is possible to work out a brief general picture of the overall physics by considering separately the problem of an isolated backward-facing step and that of an isolated forward-facing step. The backward-facing step is a classical test case and it has been widely studied both experimentally and numerically (see, among many, the review by Simpson [12] and the recent numerical analysis in Ref. [13]). In the recent work by Lee and Sung [14], wall pressure fluctuations downstream a backward facing step were analyzed by microphone arrays and the flow physics explored by simultaneous pressure/velocity measurements. It was shown that when the flow reaches the step, a separation occurs and a reverse flow zone is generated just after the step. 5–7 H further downstream, the reattachment region reverts the flow back to a boundary layer. As was also observed in Ref. [15], the reattachment point unsteadiness is recognized as the major noise source. Less experimental studies are available on isolated forward-facing steps and it is not yet clear which fluid dynamic mechanism is associated to the main acoustic radiations. Efimtsov et al. [16], suggest that the main noise source is located at the separation point followed by a recirculation just upstream the step. Conversely, in the aeroacoustic analysis conducted in Ref. [17] on a forward–backward sequence of two steps, the largest aeroacoustic effects at the forward step are attributed to the formation of a separation bubble and reattachment downstream the step, rather than upstream of it. Furthermore, as pointed out in Refs. [18,19], pressure fluctuations at the forward-facing step wall are larger than those observed on backward-facing step wall and the overall Sound Pressure Level (SPL), might be about 10 dB larger.

In the geometrical configuration presently analyzed, see Fig. 1, a flow behavior is expected that incorporates the characteristics from both the isolated backward and forward facing steps: there will be three detachments, and three reattachment points.

The presence of two steps causes an increase in number and intensity of the noise sources with respect to the case of isolated steps. The complexity of the fluid dynamics and aeroacoustics is connected to the several geometrical parameters governing the flow and the interactions of flow structures with the wall. Furthermore, the TBL approaching the second forward-facing step is in non-equilibrium conditions. As was shown in Ref. [20], a backward-facing step induces the strongest deviation with respect to an equilibrium TBL within the low-frequency range of the acoustic spectra and such effect is still observed as far as 72 H downstream of the step. The same author shows that the velocity profiles of the unperturbed TBL are recovered

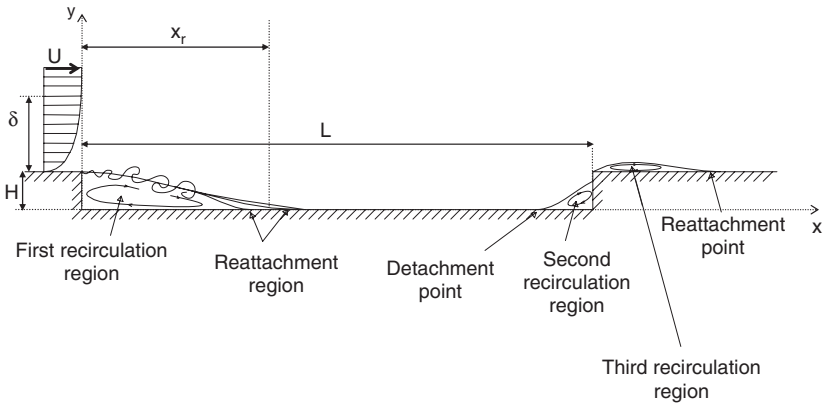

Fig. 1. Sketch of flow conditions over a backward-forward-facing step. Some relevant geometrical and kinematical parameters are also reported for clarity.

downstream the forward-step only after a distance larger than 50 H. In the present configuration, L/H is always smaller than 40, therefore it is expected that the flow that reaches the forward-facing step has not an equilibrium TBL but it should still be affected by the turbulent structures generated upstream.

The primary motivation of the present work is to cover the lack of experimental results in the case of large AR cavities and to contribute to a deeper understanding of the physics through a detailed experimental analysis. The main task of present experiments is to characterize from the aeroacoustic viewpoint the effects of the main non-dimensional parameters both on statistical quantities of interest, such as those correlated to the wall pressure fluctuations, and on the physical properties of vortical structures or unsteady physical mechanisms that are responsible for the largest wall pressure fluctuations.

Proper scaling and universal behaviors are determined by the evaluation of the overall effects of the dimensionless parameters and by a separation of variables approach. As was shown in Ref. [20], the scope of such approach is to address empirical correlations able to predict boundary layer noise emission in actual conditions (e.g. for an in-flight airplane).

The experiments have been performed in the low speed wind tunnel at ENEA (Italian National Agency for New Technology, Energy and Environment). The tunnel uncontrolled acoustically required a procedure for cleaning the wall pressure signals in the frequency domain from the background acoustic contributions. The aeroacoustic characterization is conducted by means of microphone measurements at the wall and in-flow as well as by anemometric hot wire measurements in regions of flow with no recirculations. Also simultaneous wall pressure/velocity measurements have been performed.

The proposed study is conducted parametrically on the basis of the main non-dimensional parameters governing the flow. The relevant dimensionless groups are preliminarily selected to account for the geometric and dynamic similarity requirements with respect to the full scale benchmark flow conditions, detailed in Section 2. As described in Section 3, the wind tunnel cavity model had a variable steps height and streamwise separation. Also the incoming TBL thickness has been varied by inserting curved screens at the test section inlet. Both the natural and the artificially generated boundary layers have been characterized by proper preliminary validation measurements (also presented in Section 3). The main results obtained, in dimensional and non-dimensional form, as well as the universal form functions representing the SPL and spectra, are presented and discussed in Section 4.

2. Dimensional analysis

Overall effects of the wall pressure fluctuations through the cavity are estimated through SPL (see Ref. [1] for the definition). SPL gives an estimate of the total energy contained in the acquired signal since it is computed from the standard deviation p' of the fluctuating pressure signal $p(t)$. It should be stressed that the

measured wall pressure fluctuating signals $p(t)$ contain both the hydrodynamic and the acoustic pressure contributions that, according to classical interpretations (see e.g. Ref. [21]) cannot be separated. Detailed information about the frequency content of the pressure signals is instead retrieved from the power spectra densities (PSD) of the pressure signals and denoted henceforth with the symbol $G_{pp}(f)$ (see Ref. [22] for the analytical definitions).

The dimensional analysis is aimed at determining the independent, significant dimensionless parameters in terms of which PSD and SPL would be represented. Furthermore, this analysis was needed in order to properly design the cavity model and to define the experimental measurements test matrix. To this extent, a fundamental step is to choose appropriately the velocity scale for this problem (see Ref. [20]). In a recent work, Ref. [23], a good collapse of the wall pressure spectra has been achieved downstream a backward-facing step by adopting as velocity scale the maximum mean streamwise velocity measured above the step edge. In the present geometrical configuration two different velocity scales have to be introduced in order for the incoming TBL properties to be accounted for. The first one characterizes the potential flow and it is defined as the free stream velocity U measured far from the wall and external with respect to the wall boundary layer. The second one characterizes the TBL properties and accounts for the turbulence level. This second velocity scale is defined as:

$$\tilde{u} = \frac{1}{\delta}\int_0^{\delta} u' \,\mathrm{d}y, \tag{1}$$

where δ is the Blasius boundary layer thickness, and u' the longitudinal velocity standard deviation. The choice of this velocity scale appears sensible, since, in a separating–reattaching flow, the aeroacoustic properties are more influenced by the turbulence level of the flow close to the wall rather than by other characteristic velocity scales, such as the friction velocity, whose influence seems less important. In fact, in the present geometry, the flow separation is not natural but it is imposed by the presence of the steps edge. Another possibility is to adopt as a reference velocity the maximum value of u' but, in view of the analysis of artificially generated boundary layers, this choice has been checked to be less effective in the present applications.

The dimensional analysis leads to seven independent non-dimensional groups that are here summarized to clarify the adopted symbols:

$$G'_{pp} = \frac{G_{pp}U}{q^2 H},$$

$$St_H = \frac{fH}{U},$$

$$Re_H = \frac{UH}{\nu},$$

$$\gamma = \frac{\tilde{u}}{U},$$

$$x' = \frac{x}{H},$$

$$\Delta = \frac{\delta}{H},$$

$$\Lambda = \frac{L}{H}. \tag{2}$$

The geometrical parameters (H, L) were defined in Fig. 1, ρ and ν are, respectively, the density and the kinematic viscosity, the independent variables x and f are the streamwise coordinate and the frequency and q denotes the free stream dynamic pressure $\rho U^2/2$. From Eq. (2) it is possible to define the SPL′ corresponding

to G'_{pp}, as follows:

$$\mathrm{SPL}' = 10\log_{10}\left[\int_0^{St_{H\max}} G'_{pp}\,\mathrm{d}St_H\right]. \tag{3}$$

As will be pointed out below, the normalization giving G'_{pp} and SPL′ is the conventional one. However, an improved version will be proposed to gain a more general and reliable collapse of the spectral data.

3. Experimental set-up, flow conditions and post-processing technique

3.1. Wind tunnel and the cavity model details

The experimental measurements have been conducted in the closed circuit low speed wind tunnel of the Aerodynamic Laboratory at the Energy Department of ENEA (Italian National Agency for New Technology, Energy and Environment). A sketch of the facility is shown in Fig. 2. The test section is $0.9 \times 1.16\,\mathrm{m}^2$ in cross-section and is 2.5 m long. The maximum mean velocity along the centerline of the test section is 90 m/s. The Relative Turbulence Level at 40 m/s is RTL = 0.1% with a SPL = 100 dB. The acoustic properties of the facility have been accurately qualified by several measurements with microphones. At a test section velocity of 40 m/s, the background noise of the plant presents the maximum of energy around a well-defined harmonic (~300 Hz, see Ref. [24]), which is due to vibrations induced by the fan cooling system. As it will be described in the following, a compensation technique allows to reduce the background noise contribution from the spectral records.

The main element of the backward–forward-facing step model used in present experiments is an aluminum sliding plate assembled under the test section, as diagrammatically shown in Fig. 3. The sliding plate is translated by means of a numerically controlled micrometric traversing system driven by a stepping motor. This allows the streamwise position of the wall microphones to be varied to ±1/100 mm along the full length of the cavity floor. Accounting for the preliminary dimensional analysis (Section 2) also the steps height and the streamwise opening of the cavity could be varied.

3.2. Instrumentation and acquisition parameters

The wall pressure measurements were made by using a 1/8-inch Brüel & Kjær microphone flush mounted at the wall. The microphone was located under the sliding plate, inserted into a suitably designed cavity which is sketched in Fig. 4. A small diameter pin-hole is used to connect the microphone cavity to the wall surface. The

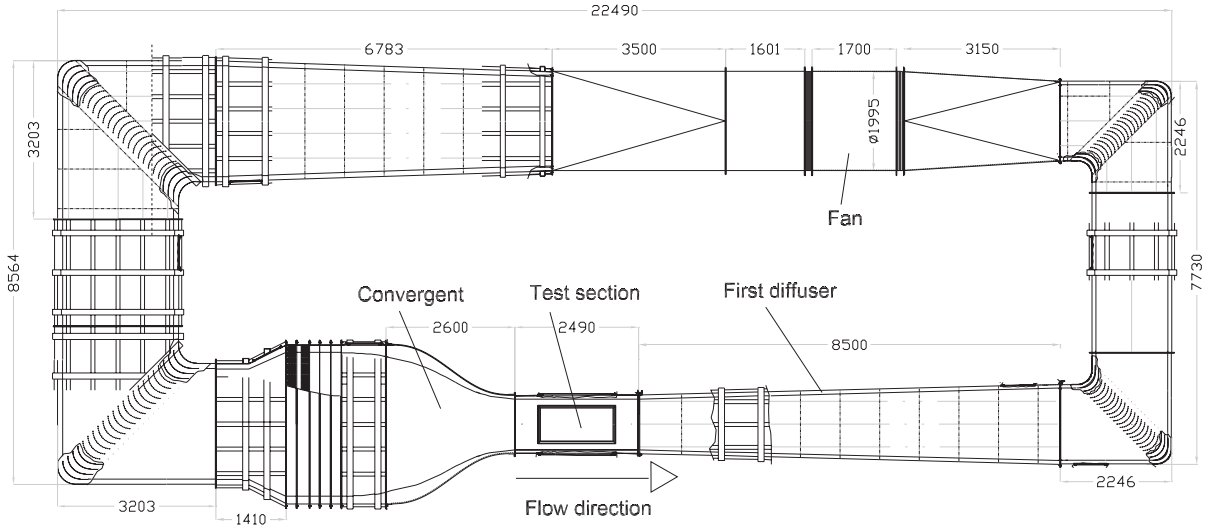

Fig. 2. Plan view of the wind tunnel facility.

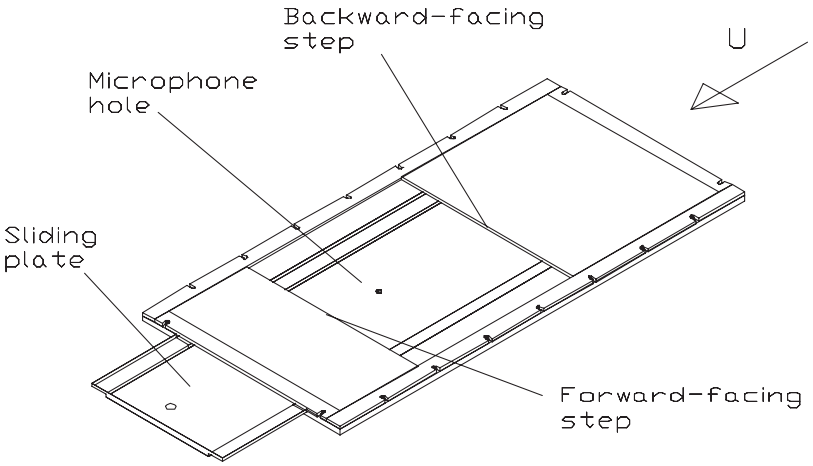

Fig. 3. Scheme of the two-steps model placed at the floor of the test section of the wind tunnel.

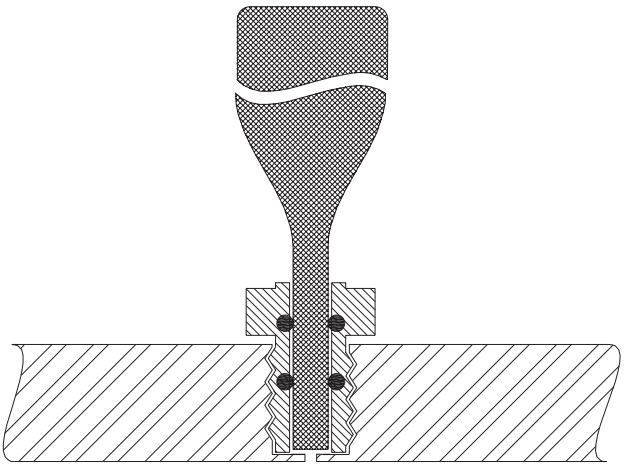

Fig. 4. Scheme of the microphone cavity and the pin-hole. The microphone is mounted through a properly designed connector. The pin-hole diameter is 1 mm and volume of the resonant cavity is 10.2 mm^3.

pinhole helps to minimize spatial averaging effects on the wall TBL wall pressure fluctuation measurements. Following Ref. [1], the Helmholtz resonance frequency of the microphone pin-hole has been estimated and resulted to be of about 6.8 kHz, thus not affecting the range of frequencies of interest. Indeed, the acquired pressure signals are low-pass filtered with a cut-off frequency of 5 kHz. An in-flow 1/8-inch Brüel & Kjær microphone, adapted with a nose-cone, was also installed in order for the back ground noise contribution to be measured and, as will be described in the following subsections, to be eliminated from the wall pressure PSD. Both the in-flow and the wall microphones were connected to pre-amplifiers and to a signal conditioner Brüel & Kjær NEXUS 2690.

Anemometric measurements were made to determine mean and r.m.s. velocity profiles of the incoming TBL as well as to characterize the velocity fluctuations in specific in-flow positions conditioned on simultaneous wall pressure signals. The velocity measurements were made by TSI3939 hot wire probes of 1 mm length and 15 μm diameter, connected to an IFA300 TSI CTA main frame.

Both velocity and pressure signals were acquired using an 8 channel Yokogawa Digital Scope DL708E. Around 10^5 samples were acquired from each channel, with a sampling rate of 20 kHz and a cut-off frequency filter at 5 kHz, to avoid aliasing effects. The filter roll-off is 92 dB/decade.

3.3. Natural and artificial TBL

It is important to study the effect of the TBL thickness on the cavity flow since, in real applications, such as along aircraft fuselages, the Blasius thickness (δ) ranges from few millimeters up to a few tens centimeters. This study aims to cover representatively such range of δ. However a relevant problem encountered in the present experiment was the artificial generation of a thick TBL over a short streamwise length.[1] This task could not be pursued by standard methods, such as by tripping the boundary layer transition, but suitable devices had to be inserted within the wind tunnel. Preliminary tests had given indication that the positioning of TBL generators, like cones, wedges, cylinders, in the still chamber does not guarantee a thick and smooth velocity profile at the test section and increased also the turbulence intensity of the potential flow. Following Ref. [25], the superposition of square grids with different mesh size (within the range 10–50 mm) was tested. However, also these generators do not give a smooth TBL profile. Specifically, the signature of the mesh size variations was reflected in both the mean and r.m.s. velocity profiles of the TBL. The optimum configuration for the TBL generators has been obtained following the indication of Ref. [26] who suggested the use of curved screens. Specifically, the choice of the proper screen (in terms of porosity, curvature and height) has been dictated by the following requirements: (i) Velocity profile with approximately a logarithmic trend; (ii) TBL Blasius thickness of the order of or larger than, 100 mm; (iii) A relative turbulence level of the order of 10–12% close to the wall decreasing towards the free stream; (iv) A limited perturbation of the free stream. Adopting a proper synthesis procedure, a curved screen with curvature radius $R_c = 500$ mm have been commissioned and positioned 0.40 m before the convergent end section. The acoustic disturbances due to the screens have been also evaluated by measurements with microphones. It has been checked that the free stream SPL and PSD are weakly affected by the insertion of the curved screen.

Both the artificial and the natural TBL have been characterized in terms of mean velocity and turbulence level profiles as well as Blasius and displacement thickness (δ_1) for different free stream velocities. Some results are reported in Fig. 5 at a free stream velocity of 10 m/s with and without the curved screen. These show that the artificial TBL has a profile similar to the natural one (see e.g. Ref. [27]). The achieved Blasius thickness for the natural and artificial TBL reported in the figure are respectively $\delta \simeq 22$ mm and $\delta \simeq 165$ mm. The friction velocity U_τ used for scaling on inner variables has not been directly measured but has been estimated a-posteriori from the integral streamwise momentum balance of the boundary layer flow. Therefore the plots reported in panel (b) of Fig. 5 have only qualitative meaning but the satisfactory collapse observed indicates that the logarithmic profile is approximately reproduced also by the artificial boundary layer. The U_τ/U ratios achieved in the reported cases are $\simeq 0.043$ and $\simeq 0.031$ for the natural and artificial TBL, respectively. Considering the whole range of flow conditions analyzed, the achieved Blasius thickness of the artificial TBL ranges from ~100 to ~165 mm, depending on the free stream velocity. Further TBL details are given in the next subsection.

3.4. Flow conditions and data post-processing

The sliding cavity floor was translated along the enclosure length to measure the streamwise floor pressure fluctuations with the floor mounted microphone. The number of the measurement points along the floor was varied in the range 32–40, with a spatial resolution of $\Delta x = 8$ mm. This corresponds to $\Delta x = 0.55\,\mathrm{H}$ for the $H = 15$ mm step and $\Delta x = 0.32\,\mathrm{H}$ for the $H = 25$ mm step, respectively. Wall pressure measurements were also performed at two fixed positions downstream the forward-facing step. The geometry and flow conditions varied over a wide range during the measurement campaign. The ranges of the most relevant dimensional quantities are summarized in Table 1 while their dimensionless counterparts are reported in Table 2.

The acquired pressure signals have been post-processed to reduce the background noise. The background noise reduction procedure proposed in Ref. [28] is used to enhance the signal to noise ratio. Carley and Fitzpatrick's [28] method is based on simultaneous measurements of an in-flow reference pressure (yielding the back-ground noise contribution) and the wall pressure fluctuations. The contribution

[1] In the ENEA wind tunnel, the natural TBL thickness at the backward facing step edge in the test section is few millimeters thick and such a location is only 1 m downstream of the end of the convergent (Fig. 2).

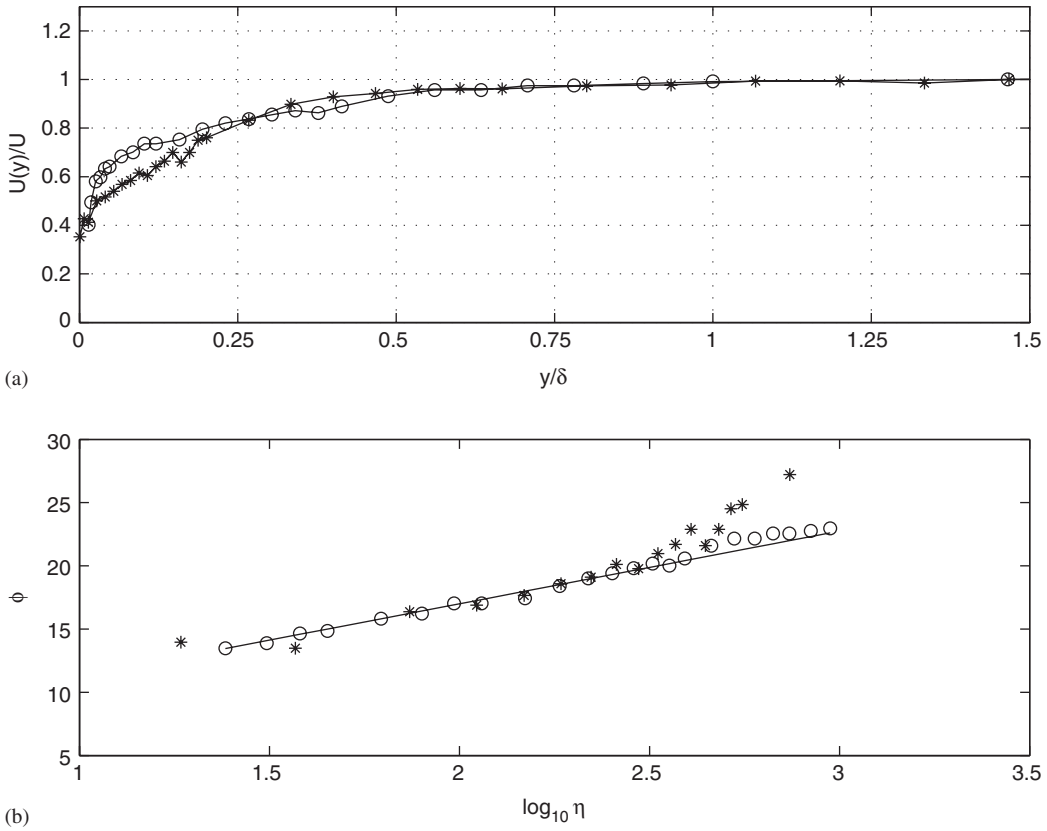

Fig. 5. Artificial (*) and natural (○) TBL obtained at a free stream velocity (U) of 10 m/s. (a) Longitudinal mean velocity profiles scaled on outer variables. (b) Semi-log plot of the longitudinal mean velocity profiles scaled on inner variables. The straight line reported in panel (b) represents the universal log-law $\phi = 5.75 \times \log_{10}\eta + 5.5$ where $\phi = U(y)/U_\tau$ and $\eta = yU_\tau/\nu$.

Table 1
Range of the main dimensional quantities

U (ms^{-1})	H (mm)	L (mm)	δ (mm)
10–50	15–25	340–640	22–165

Table 2
Range of the main dimensionless quantities. Re_H and St_H were defined in Eq. (2) while $Re_\delta = \frac{U\delta}{\nu}$

Re_H ($\times 10^4$)	Re_δ ($\times 10^4$)	$\Lambda = L/H$	$\Delta = \delta/H$	St_H	Ma
10–86	1.9–56.5	13.6–42.7	1–13	10^{-3}–10	0.03–0.15

of the background noise as well as of the pressure fluctuation which is coherent through the domain, is eliminated from the frequency spectra by computing the auto-spectra of both signals and their frequency coherence function. In the present analysis, the background noise contribution is measured by an in-flow microphone positioned outside the TBL. The procedure is applied to all pressure spectra measured

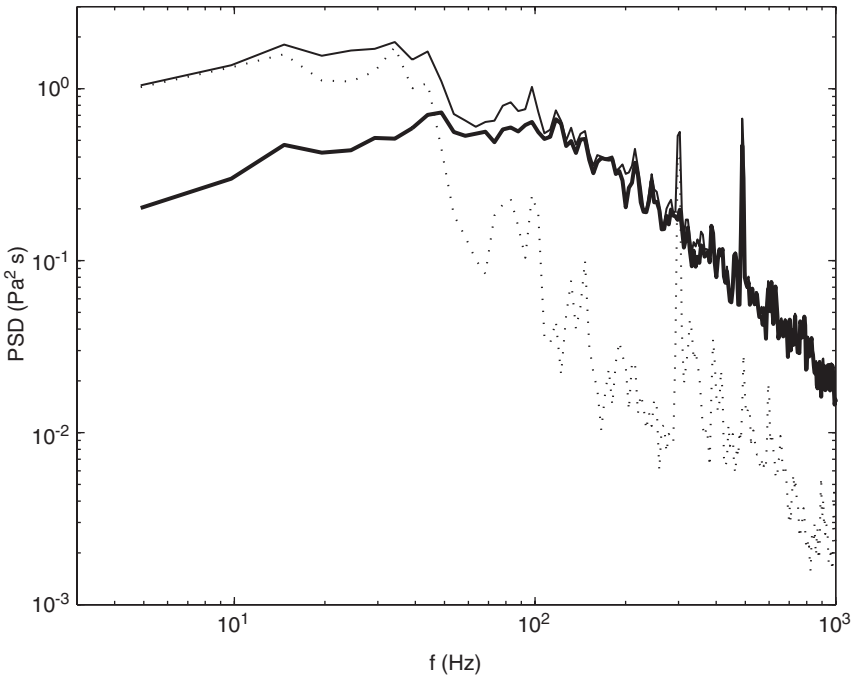

Fig. 6. Example of spectra correction for $U \simeq 50\,\mathrm{m/s}$, $H = 15\,\mathrm{mm}$ and $x' = 20$. Solid line is the original spectrum, dashed line is the background noise spectrum and the solid-bold line is the spectrum resulting from the compensation technique.

along the floor and the main outcome is the reduction of the background noise at low frequencies and at the frequency around 300 Hz where a background noise peak is present. An example of the effectiveness of the noise reduction procedure is presented in Fig. 6 where it is shown that the background noise at low frequencies as well as the harmonic at $\simeq 300$ Hz are removed from the microphone signal. A frequency peak at $\simeq 500$ Hz is instead probably due to wall vibrations and it is not eliminated, since it is not sensed by the background microphone.

In addition to the spectral estimates, the aeroacoustic nature of the wall pressure fluctuations is further explored by the application of two conditioning procedures, denoted as auto-conditioning and cross-conditioning, that are briefly described in the following.

3.4.1. Auto-conditioning procedure

The auto-conditioning procedure is based on the wavelet transform of the wall pressure signals, in order for the most energetic non-periodic contributions to be extracted. The choice of the wavelet technique is motivated by the fact that the wavelet decomposition, in spite of the Fourier transform, permits to represent a generic signal simultaneously in terms of a translation time (t) and a resolution time scale (r) whose inverse corresponds to the frequency (f).

The wavelet decomposition is accomplished by projecting the acquired signal over basis of compact support functions, i.e. localized both in the time domain and in the transformed space. We note that in the Fourier decomposition the projection is performed over trigonometric functions, so that the physical information is spread over a theoretically infinitely extended time domain. Localized events are therefore missed by the Fourier decomposition while they are correctly retrieved by the wavelet transform through the representation of the signal over the time-frequency domain.

The wavelet based method adopted in the present analysis is the one proposed in Refs. [29,30]. It is based on the decomposition of the pressure signal by the orthonormal discrete wavelet transform, [31]. The wavelet expansion is performed by a Fast-Wavelet-Transform algorithm using Battle–Lemarie *Mother* wavelet $\Psi(t)$ (see e.g. Ref. [32]). Formally, the wavelet transform of the signal $p(t)$ at the resolution time scale r

is given by the following expression [33]:

$$w(r,t) = C_{\Psi}^{-1/2} r^{-1/2} \int_{\infty}^{\infty} \Psi^{*}\left(\frac{t-\tau}{r}\right) p(\tau)\,\mathrm{d}\tau, \tag{4}$$

where $C_{\Psi}^{-1/2}$ denotes a coefficient which accounts for mean value of $\Psi(t)$, and the integral represents a covolution between $p(t)$ and the dilated and translated complex conjugate counterpart of $\Psi(t)$.

The events tracking method is based on the computation of the so called Local Intermittency Measure (LIM) (see Ref. [33]) defined as:

$$l(r,t) = \frac{[w(r,t)]^2}{\langle [w(r,t)]^2 \rangle_t}, \tag{5}$$

where the symbol $\langle\cdot\rangle_t$ denotes a time average. The LIM amplitude, that is a normalized version of the square of the wavelet coefficients, is the threshold to trigger the events which are selected to perform an ensemble average of the original pressure signal [29]. Indeed, peaks of LIM represent large contribution of pressure variations to the overall SPL. An example of the LIM distribution obtained from a test signal is reported in Fig. 7. The white regions of the 2D plot correspond to large amplitude of LIM which are associated to large, local in time, pressure fluctuations. The LIM thresholding thus allows the selection of these events. It is worth

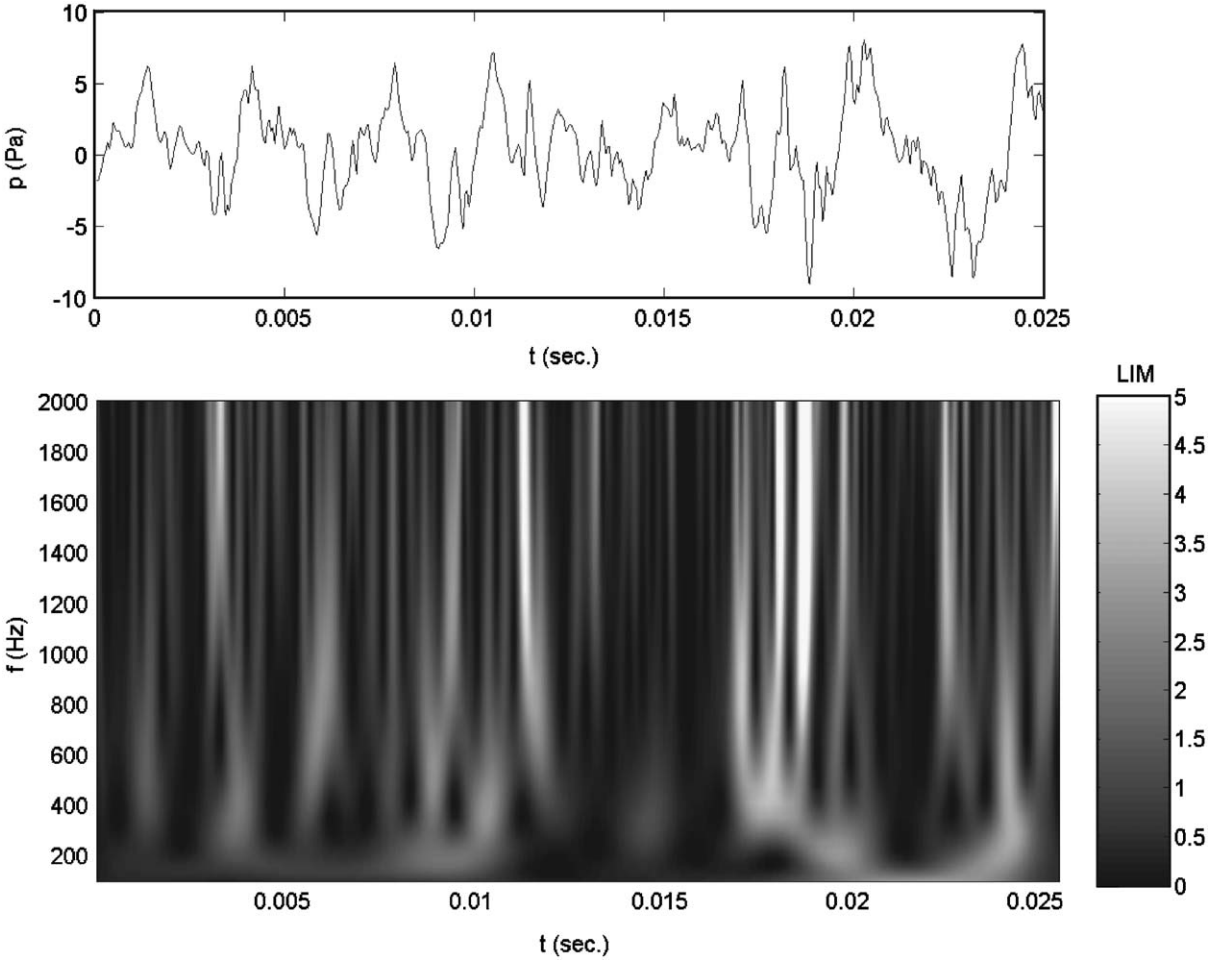

Fig. 7. Example of LIM distribution computated from a segment of an acquired pressure signal.

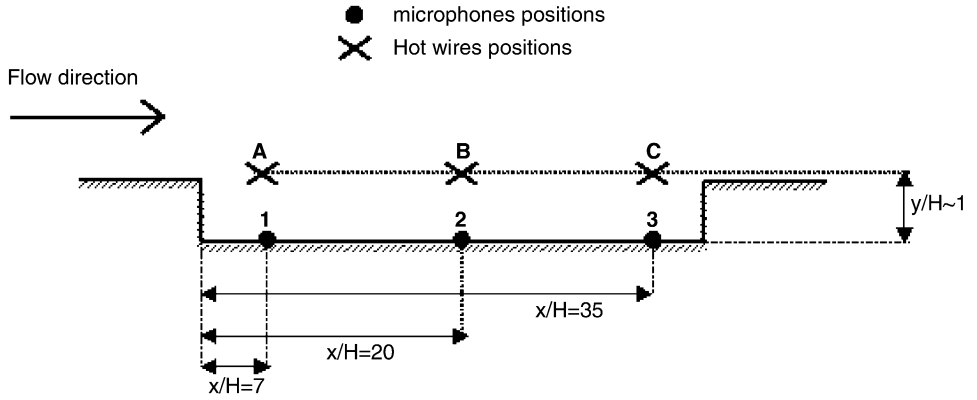

Fig. 8. Locations of the microphones and hot wire probes for the simultaneous velocity/pressure measurements. Note that simultaneous measurements were performed only with one microphone and the three hot wires.

noting that, according to the classical Fourier picture, local and sharp variations of $p(t)$ correspond to high frequency events.

The procedure of conditioning $p(t)$ in the wavelet space onto the events selected, leads to an averaged signature, which represents the most probable shape of the most energetic structures which were hidden in the original signal. The wavelet transform is indeed needed to recover the phase of the non-periodic and strongly non-Gaussian events that is missed by the more conventional Fourier decomposition. The ensemble averaging procedure is applied to the whole set of measured wall pressure signals thus allowing for the spatial evolution of the most energetic averaged pressure time-signatures to be analyzed. As will be shown in the next section, this method helps to clarify the nature of the events responsible for the largest pressure fluctuations at the wall.

3.4.2. Cross-conditioning procedure

The cross-conditioning analysis is conducted by simultaneous measurements of wall pressure fluctuations and streamwise velocity component. In this approach the velocity signals are conditioned on the wall pressure peaks which are selected by a proper thresholding. The procedure is detailed in Ref. [34] where it was used to study a turbulent jet. The outcome of the method is an ensemble averaged velocity signature that represents the most probable streamwise velocity fluctuation at the hot wire tip induced by the fluid dynamic event responsible for the largest pressure fluctuations at the wall. Furthermore, as it will be shown in the next section, from the ensemble averaged velocity time signature it is possible to retrieve the averaged time delay between the pressure peaks and the velocity structures which, after accounting for the convection velocity and the speed of sound, leads to an estimate of the spatial location of the structures responsible for the largest pressure peaks. For instance, and as will be shown later on, a zero time delay indicates that, on the average, the pressure peaks where the anemometer is placed, while a negative time delay indicates that the structure is sensed by the anemometer first and then it produces the pressure peak (vice-versa for a positive time delay). The measurement lay out adopted for the cross-conditioning analysis is reported in Fig. 8. Simultaneous measurements from one microphone and three hot wires were performed. Standard cross-correlations among the velocity signals and between pressure/velocity signals could be performed and results will also be presented in the next section.

4. Results and discussion

The spectral analysis and the auto- and cross-conditioning techniques described in Section 3 were applied to explore the shallow cavity flow physics and to understand the basic mechanisms responsible for the largest pressure fluctuations at the cavity floor. As pointed out in Refs. [23,35], the axial position of the first reattachment, hereafter denoted as x_R, is a relevant parameter but it is difficult to determine. In the present

work, the efficient and quantitative way proposed by Efimtsov et al. [15,16], who determines x_R from the maximum SPL, has been adopted. A separation of variables approach was then applied to determine spectra and SPL scaling in account of the main governing parameters. This analysis aims to determine empirical formulae that can be applied in practical applications to predict, within reasonable approximation, wall pressure spectra and SPL close to surface irregularities. The background noise elimination procedure described in Section 3 was applied to the whole set of wall pressure signals therefore only cleaned spectra are presented in the following.

4.1. Flow physics

The SPL distribution is of particular relevance, since it gives an indication of the location of the regions of maximum pressure fluctuations along the cavity. Examples of SPL distribution obtained at different inflow conditions are presented in Fig. 9. The SPL exhibits two maxima, the first one downstream the first step and the second one at the end of the cavity, in the vicinity of the forward-facing step. The position of the first maximum, x_R, depends on the step height H and, from the analysis of the whole data set, it results $x_R \simeq 6H$. This is confirmed by Fig. 10 where the normalized SPL′, defined in Eq. (3), are reported in terms of the normalized abscissa $x' = x/H$ showing a good collapse of the streamwise positions of the first maximum. From this figure, the effect of the streamwise cavity aspect ratio $\Lambda = L/H$ on SPL′ can also be appreciated. It

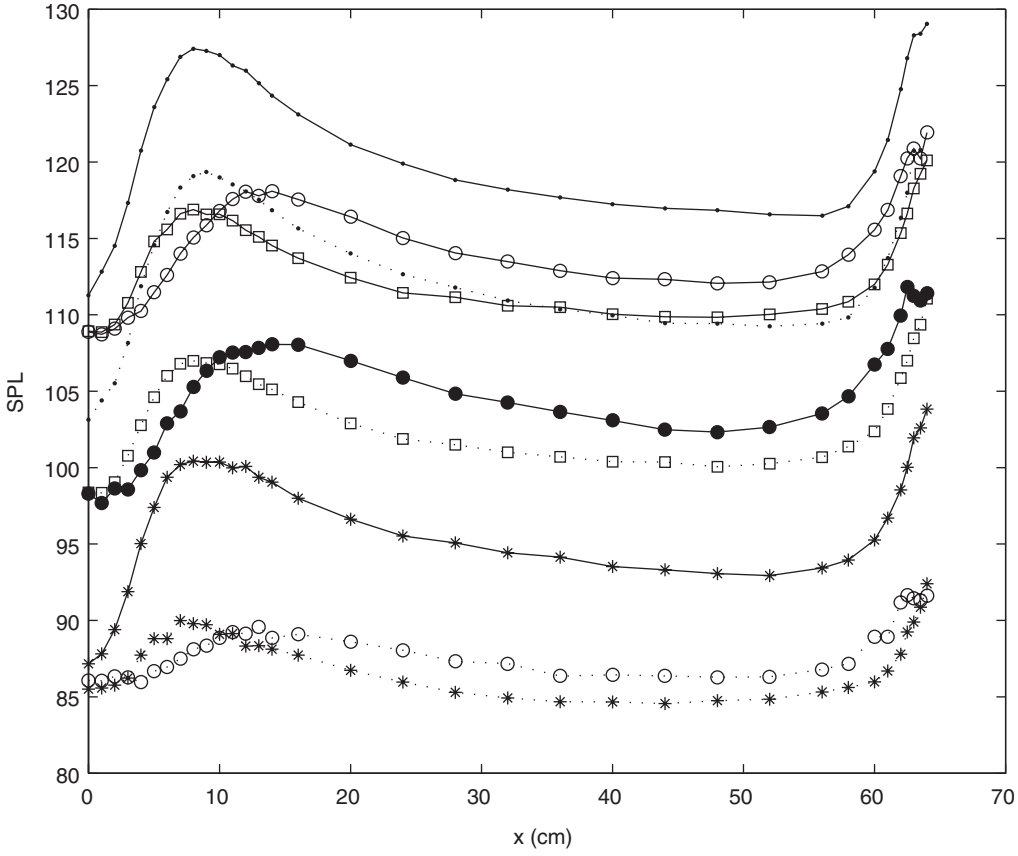

Fig. 9. SPL distribution along the cavity for the following flow conditions: $U = 10\,\mathrm{m/s}$, $H = 15\,\mathrm{mm}$, $L = 640\,\mathrm{mm}$ (symbol '✻' on dotted line); $U = 30\,\mathrm{m/s}$, $H = 15\,\mathrm{mm}$, $L = 640\,\mathrm{mm}$ ('□' on dotted line); $U = 50\,\mathrm{m/s}$, $H = 15\,\mathrm{mm}$, $L = 640\,\mathrm{mm}$ ('□' on solid line); $U = 10\,\mathrm{m/s}$, $H = 15\,\mathrm{mm}$, $L = 640\,\mathrm{mm}$ ('○' on dotted line); $U = 30\,\mathrm{m/s}$, $H = 25\,\mathrm{mm}$, $L = 640\,\mathrm{mm}$ ('●' on solid line); $U = 50\,\mathrm{m/s}$, $H = 25\,\mathrm{mm}$, $L = 640\,\mathrm{mm}$ ('○' on solid line); $U = 10\,\mathrm{m/s}$, $H = 15\,\mathrm{mm}$, $L = 640\,\mathrm{mm}$, Natural TBL ('✻' on solid line); $U = 30\,\mathrm{m/s}$, $H = 15\,\mathrm{mm}$, $L = 640\,\mathrm{mm}$, Natural TBL ('·' on dotted line); $U = 50\,\mathrm{m/s}$, $H = 15\,\mathrm{mm}$, $L = 640\,\mathrm{mm}$, Natural TBL ('·' on solid line).

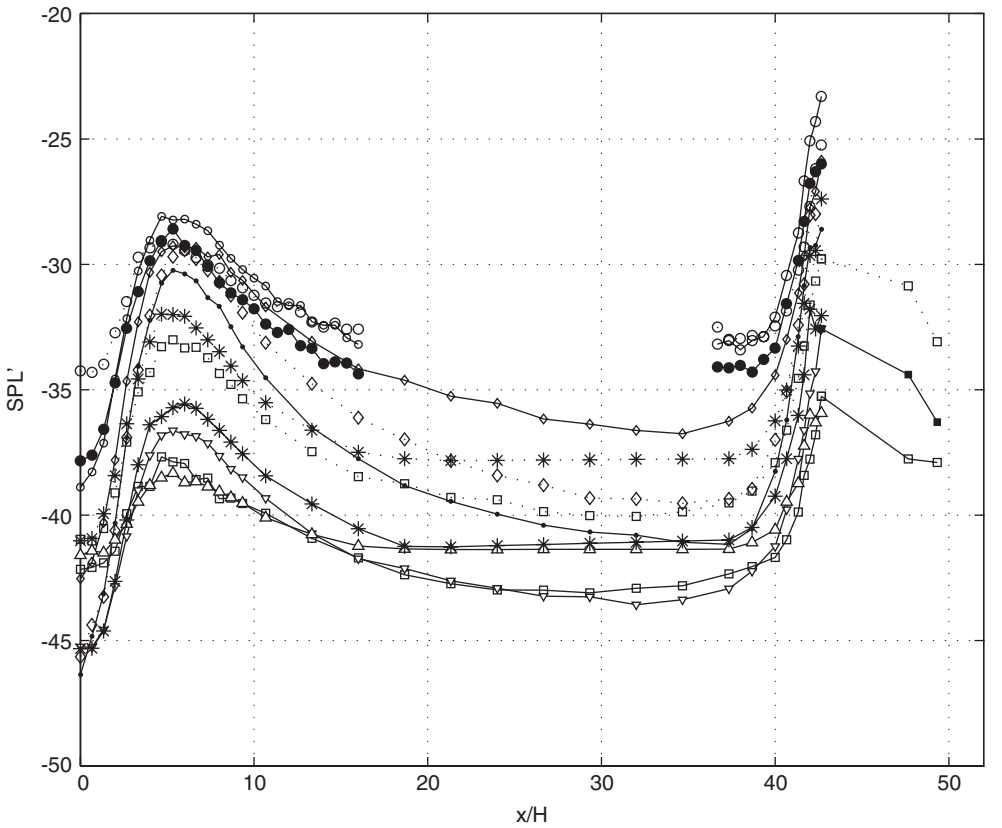

Fig. 10. SPL′ vs. x' distribution along the cavity at different inflow conditions. For three cases, measurements downstream the second step are also reported. The flow conditions considered and the corresponding symbols adopted are the following: $U = 10\,\mathrm{m/s}$, $H = 15\,\mathrm{mm}$, $L = 340\,\mathrm{mm}$ (symbol '○' on dotted line); $U = 30\,\mathrm{m/s}$, $H = 15\,\mathrm{mm}$, $L = 340\,\mathrm{mm}$ ('○' on solid line); $U = 50\,\mathrm{m/s}$, $H = 15\,\mathrm{mm}$, $L = 340\,\mathrm{mm}$ ('•' on solid line); $U = 10\,\mathrm{m/s}$, $H = 15\,\mathrm{mm}$, $L = 640\,\mathrm{mm}$ ('▽' on solid line); $U = 50\,\mathrm{m/s}$, $H = 15\,\mathrm{mm}$, $L = 640\,\mathrm{mm}$ ('□' on dotted line); $U = 10\,\mathrm{m/s}$, $H = 15\,\mathrm{mm}$, $L = 640\,\mathrm{mm}$, Natural TBL ('◇' on solid line); $U = 30\,\mathrm{m/s}$, $H = 15\,\mathrm{mm}$, $L = 640\,\mathrm{mm}$, Natural TBL ('◇' on dotted line); $U = 50\,\mathrm{m/s}$, $H = 15\,\mathrm{mm}$, $L = 640\,\mathrm{mm}$, Natural TBL ('·' on solid line). $U = 10\,\mathrm{m/s}$, $H = 25\,\mathrm{mm}$, $L = 640\,\mathrm{mm}$ ('△' on dotted line); $U = 30\,\mathrm{m/s}$, $H = 25\,\mathrm{mm}$, $L = 640\,\mathrm{mm}$ ('✻' on solid line); $U = 50\,\mathrm{m/s}$, $H = 25\,\mathrm{mm}$, $L = 640\,\mathrm{mm}$ ('✻' on dotted line).

is observed that a similarity in shape is always exhibited independently from the inflow conditions and geometry thus suggesting that a collapse of the curves can be obtained by a proper rescaling. According to Ref. [15], the normalized location of the first maximum x_R/H is weakly dependent from the flow conditions and geometry and corresponds to the average position of the reattachment point of the separation bubble downstream the backward-facing step. A reattachment location of $x' \simeq 6$ was documented also by other authors (e.g. Ref. [14]) for the case of an isolated backward-facing step. More generally, the large body of literature on this aspect (see e.g. the review paper by Eaton and Johnston [36]) shows that the state of the separating boundary layer (whether laminar or turbulent), its normalized thickness δ/H and the presence of spanwise boundaries, B/H, do change x_R/H within the range 5–7 H. Fig. 11 compares the reattachment pressure field recorded in this study against the published literature [37–39]. It is shown that the maximum of p' which, by definition gives the maximum of SPL, corresponds to the reattachment position. As was shown in Fig. 10 it is therefore possible to conclude that the presence of the downstream step does not affect significantly the flow physics at the upstream step which behaves essentially as an isolated backward-facing step. This conclusion is supported by the spectral analysis reported in Fig. 12 where the PSD computed at $x' = 6$ are compared with previous results obtained at the reattachment point downstream backward-facing steps, showing a good agreement.

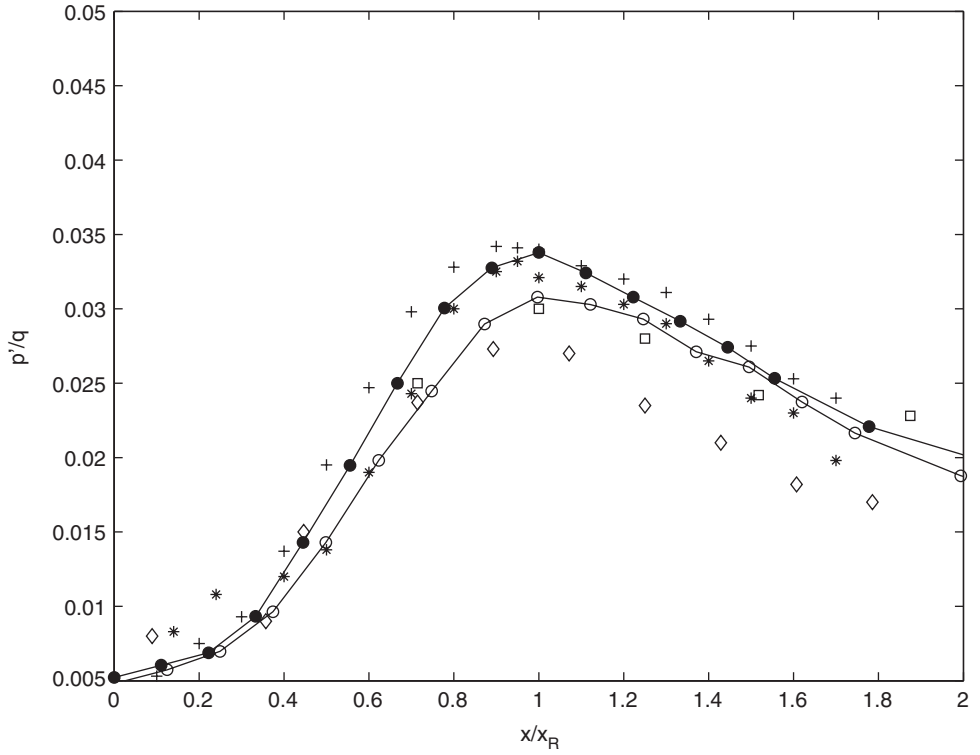

Fig. 11. Evolution of the normalized wall pressure standard deviation as a function of the distance from the backward-facing step normalized with respect to the reattachment length x_R. For the present cases, x_R is assumed to correspond to the first maximum of the SPL at the wall (see Fig. 9). Present cases are solid lines with '•' symbol ($H = 15$ mm and $U = 30$ m/s) and '○' symbol ($H = 15$ mm and $U = 50$ m/s). '□' symbols are results from Ref. [23], '+' from Ref. [37], '◇' from Ref. [38], and '✻' from Ref. [39].

According to the observations of Farabee [20], sound generated by the backward-facing step is mainly sensed within the low frequency range of the wall pressure spectra. This effect is shown in Fig. 13 where a spectrogram of Gpp' is reported for $U = 30$ m/s, $H = 15$ mm and $\delta \simeq 25$ mm. It can be observed that the low frequencies energy is significantly increased at the reattachment position corresponding to $x' \simeq 6$. Similar results are obtained from other test cases and are not reported for brevity.

According to the SPL distributions of Figs. 9 and 13, an increase of energy is observed also when the second step is approached and within approximately the same frequency band of the SPL peak at x_R. The main effect of the second step is to increase the overall acoustic level that, as was observed in Figs. 9 and 10, leads to SPL amplitudes larger than those measured at the first reattachment point x_R. This indicates that from the acoustic viewpoint the forward-step is more effective in emitting noise than the backward-step. This aspect is very important from a practical viewpoint, since any strategy aimed at abating the overall noise has to be focused towards controlling the dominant noise sources at the foreward facing step.

The physical mechanism underlying the second maximum is presently interpreted as an effect of the impact of flow structures on the vertical face of the step [16]. Indeed, at the low speeds presently considered, the main physical mechanism producing the largest pressure fluctuations at the wall is likely to be the space coherent unsteady surface pressure fluctuation at the downstream wall. As indicated e.g. in Ref. [40], this dipole type contribution is expected to prevail on the flow self noise commonly present in shallow cavities at higher Mach numbers (see e.g. Refs. [41,42]), which is expected to make a lower contribution to the overall SPL. This localizes the main noise sources at the rear wall. This interpretation is supported by results reported in Fig. 10 where some of the $\mathrm{SPL}'(x')$ distributions reported include two measurement points located downstream of the second step. It is shown that after the second (forward-facing) step the SPL decreases thus indicating that the

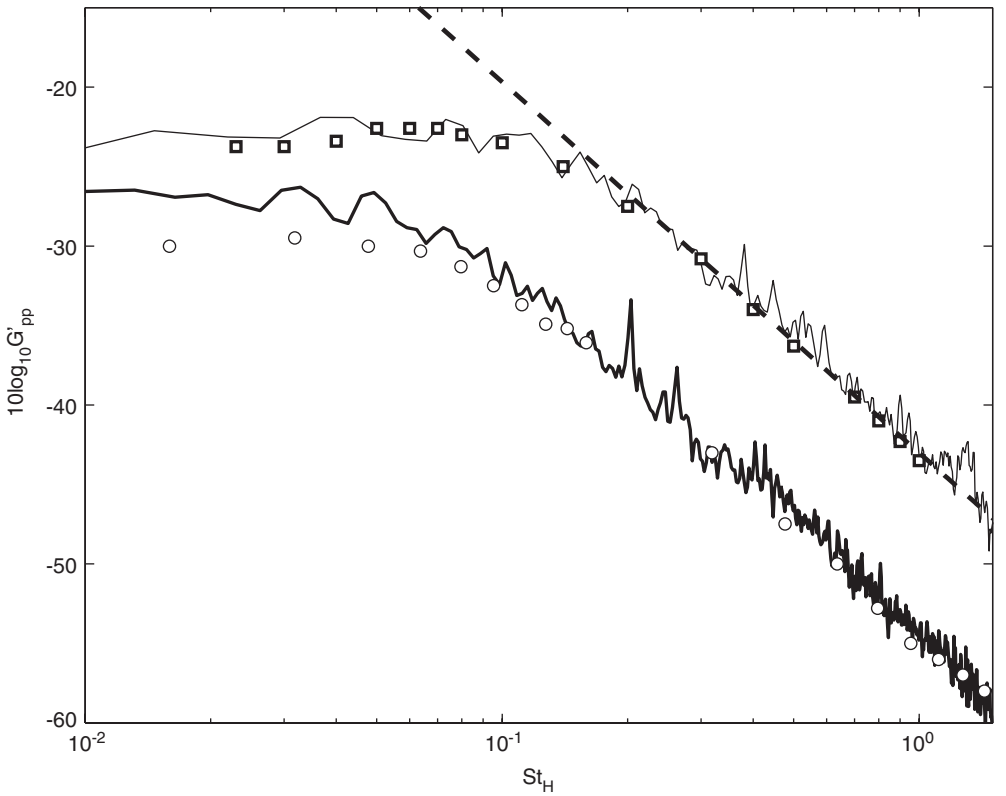

Fig. 12. Validation of the normalized PSD (Gpp') close to the first step. Solid bold line corresponds to present results at $X/H = 6$ and $U = 30\,\mathrm{m/s}$. Solid line corresponds to present results at $X/H = 6$ and $U = 10\,\mathrm{m/s}$. Symbols '□' correspond to results from Ref. [23] while '○ are from Ref. [17]. The dashed line denotes the reference curve $f^{-7/3}$ typical of boundary layer pressure fluctuations (see also Ref. [14]).

largest pressure fluctuations are generated very close to the vertical face of the forward step. Further support to this physical interpretation is given by the analysis of results obtained from the auto- and cross-conditioning methods described in Section 3.

Within the framework of the present interpretation, the physical mechanisms underlying the SPL peaks at the first reattachment position and at the forward step, should be different. This hypothesis is supported by the analysis of the data with the post-processing methods presented in the previous section. The wavelet-based auto-conditional averaging method has been applied to the wall pressure signals so that the evolution of the averaged time signature of the most energetic pressure structures have been analyzed in terms of x'. As a preliminary test, the averaging method was applied to the pressure signal obtained from the inflow microphone far from the wall and thus far from the noise sources. In this case, a clear averaged pressure structure was not detected indicating that, as expected, in the external flow, the acoustic effects are not due to coherent events but rather to random uncoherent fluctuations.

Examples of the pressure signatures resulting from the application of the auto-conditioning method to the wall pressure signals are presented in Fig. 14 whereas a 3D plot showing the overall evolution is reported in Fig. 15. Similar results are obtained in the other test cases and are not reported for brevity. The different behaviors observed at different x' allows for various regions to be identified. Different regions correspond to different physical effects which can be ascribed to the influence of vortices shed from the backward-facing step which may move along the stagnation streamline and reach the reattachment position or may be convected past the stagnation point. Starting from the reattachment region, in the position $x' \simeq 6$ a large negative pressure peak is detected. This can be interpreted as the signature of concentrated vortices since within the vortex cores at high vorticity magnitude the pressure reaches a minimum and sufficiently close to the wall the

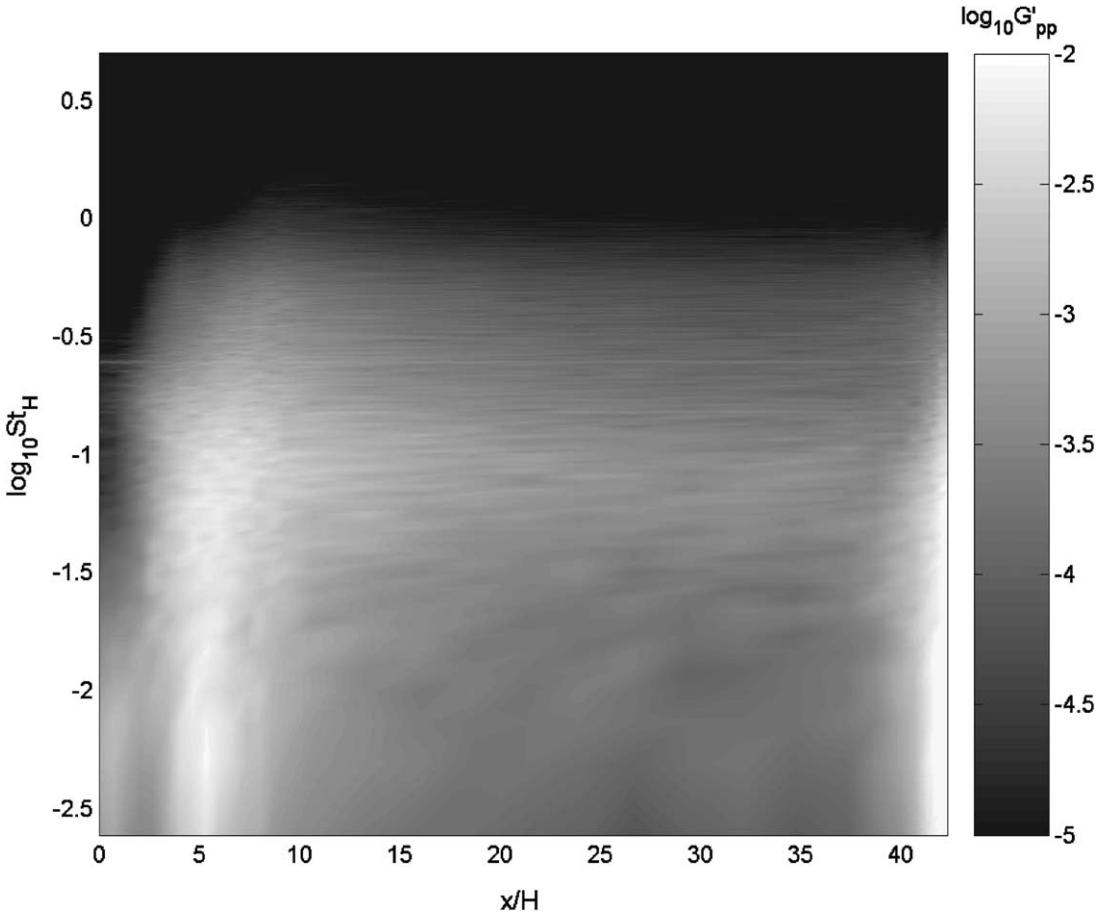

Fig. 13. Spectrogram of G'_{pp} for $U = 30\,\mathrm{m/s}$ and $H = 15\,\mathrm{mm}$ (Natural TBL). A lighter region indicates large energy content.

pressure core minimum is detected by the microphone. At $x' = 4.7$ a transition showing a positive–negative sequence of pressure peaks is observed which accounts for the vortex core effect and the increase of pressure due to the induced velocity outside the vortex core. The negative delay of the negative pressure peak due to the vortex core effect substantiates the circumstance that the induced velocity anticipates the vortex core effect. Finally, for positions further upstream (about $2 < x' < 4.5$) only the induced velocity effect (positive pressure peak) survives.

The intermediate region between the two steps does not show any structure whereas a weaker negative structure is detected very close to the second step. The separation point close to the downstream step therefore does not show a behavior similar to the upstream step reattachment. The overall ensemble averaged pressure tracks reported in Fig. 15 confirm that the pressure modes detected close to the upstream step have a larger amplitude with respect to those in the vicinity of the downstream one, in contrast with the SPL evolution which shows an opposite trend. This result seems to indicate that the increase in magnitude of the SPL distribution close to the downstream step is not due to unsteady fluid dynamic events but, according to the interpretation given in Ref. [16], it has to be attributed to pure acoustic effects probably due to the impact of flow structures on the vertical side of the forward step.

Fig. 16 presents the velocity/velocity cross-correlation coefficients obtained from the three anemometer placed close to the cavity wall, as sketched in Fig. 8. A peak is observed only in correlations involving the signal from anemometer A, that is closest to the upstream step. The ratio of the spatial separation between the anemometers and the time delays τ of the cross-correlation peaks (for both ρ_{AB} and ρ_{AC}) gives an average

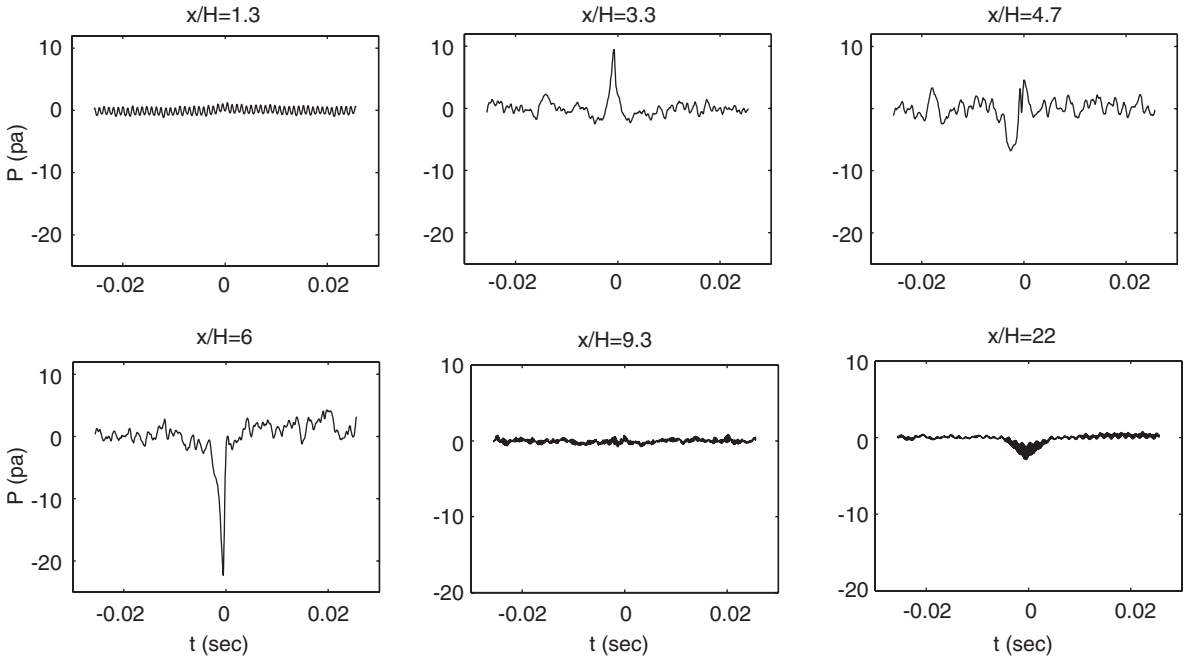

Fig. 14. Shape of the averaged wavelet-educed pressure structure for various positions along the cavity. $U = 30\,\mathrm{m/s}$, $H = 15\,\mathrm{mm}$ and $\delta \simeq 25\,\mathrm{mm}$.

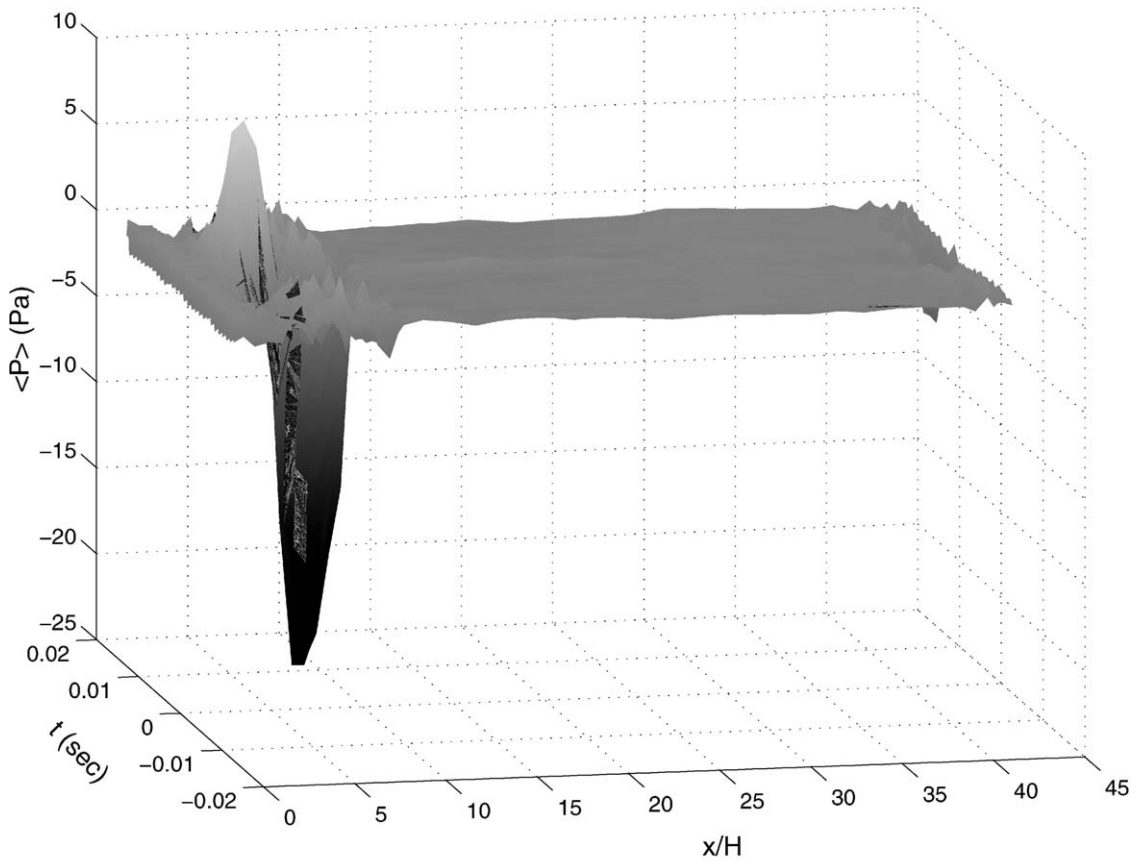

Fig. 15. Overall evolution along the cavity of the averaged wavelet-educed pressure structure for the same conditions of Fig. 15.

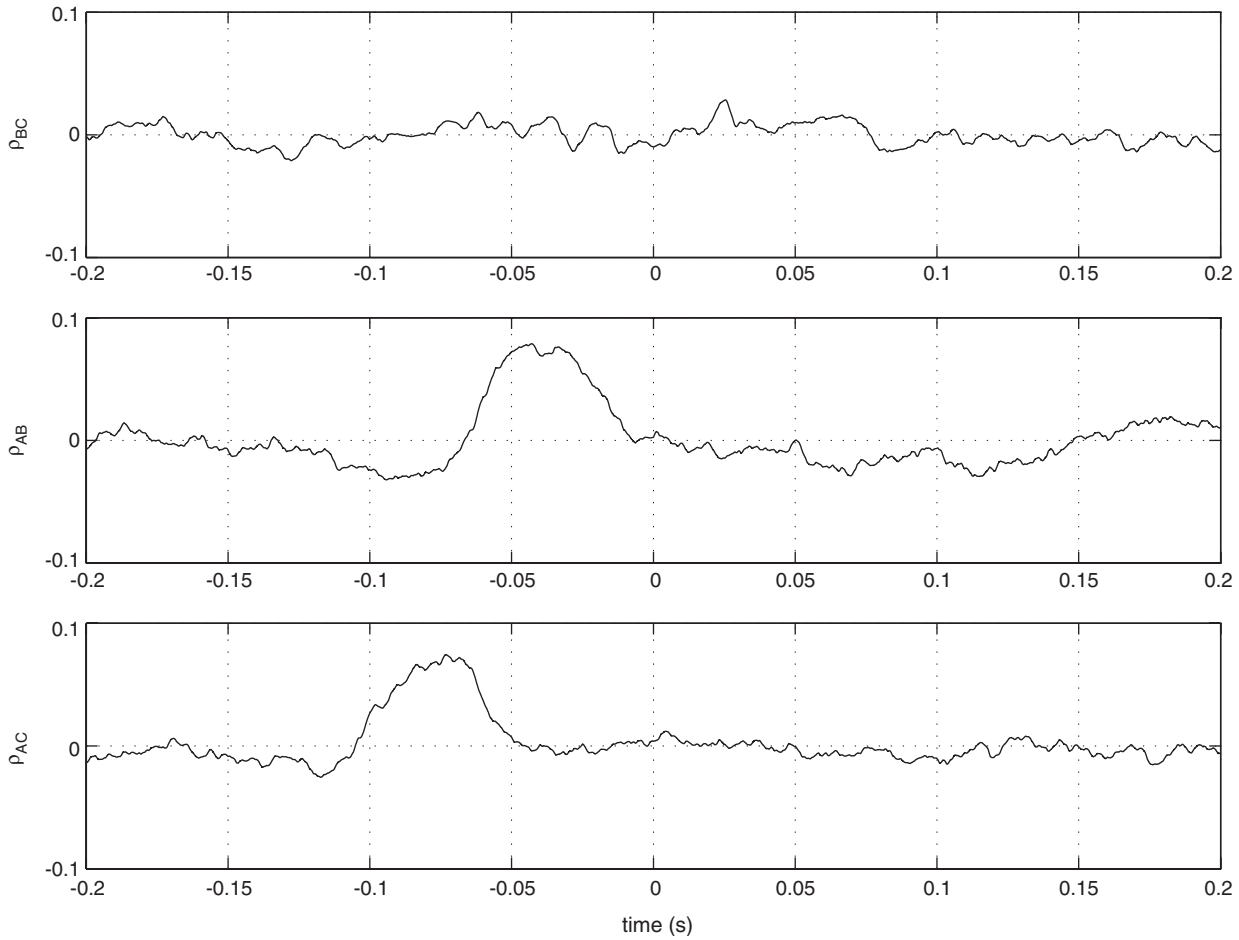

Fig. 16. Cross correlation coefficients computed between pairs of signals obtained from anemometers A, B and C reported in Fig. 8. The delay times are -0.04 s and -0.08 s for ρ_{AB} and ρ_{AC}, respectively. Flow conditions are: $U = 10$ m/s, $H = 15$ mm, $L = 640$ mm and $\delta = 25$ mm.

convection velocity (U_c) of $\simeq 5.5$ m/s which is equal to about 70% of the mean boundary layer velocity measured at the anemometers locations ($\simeq 8$ m/s) and 55% of the free stream velocity ($\simeq 10$ m/s). The measured convection velocity is in good agreement with the results in Ref. [14] where $U_c = 60\%$ of the free stream velocity was found. This result indicates that the aerodynamic field is characterized by coherent flow structures that are released from the upstream step, are convected downstream and survive up to the second step. The impact of those structures on the vertical side of the second step may be a significant acoustic source. This is shown in Fig. 17 where results obtained from the pressure/velocity cross-conditioning and cross-correlations are presented. A clear peak is indeed shown in the cross-correlation of the anemometer A with the pressure sensed by microphone 3, that is the one close to the downstream step. This peak corresponds to a negative time delay indicating that the structure is firstly sensed by the anemometer A (which is close to the first step) and then it reaches a location close to the microphone 3, at the vertical side of the second step, where it emits noise. No clear cross-correlation peak is instead observed between anemometer A and the microphone 2, located at an intermediate position between the two steps. This indicates that no significant correlation is present between flow structures passing by A and the wall pressure fluctuations at position 2 and that the acoustic effect of the reattachment does not influence the pressure signal perceived by the downstream microphones (2 and 3). On the other hand, the cross-correlation between the microphone 1 and the anemometer A close to the upstream reattachment point shows an

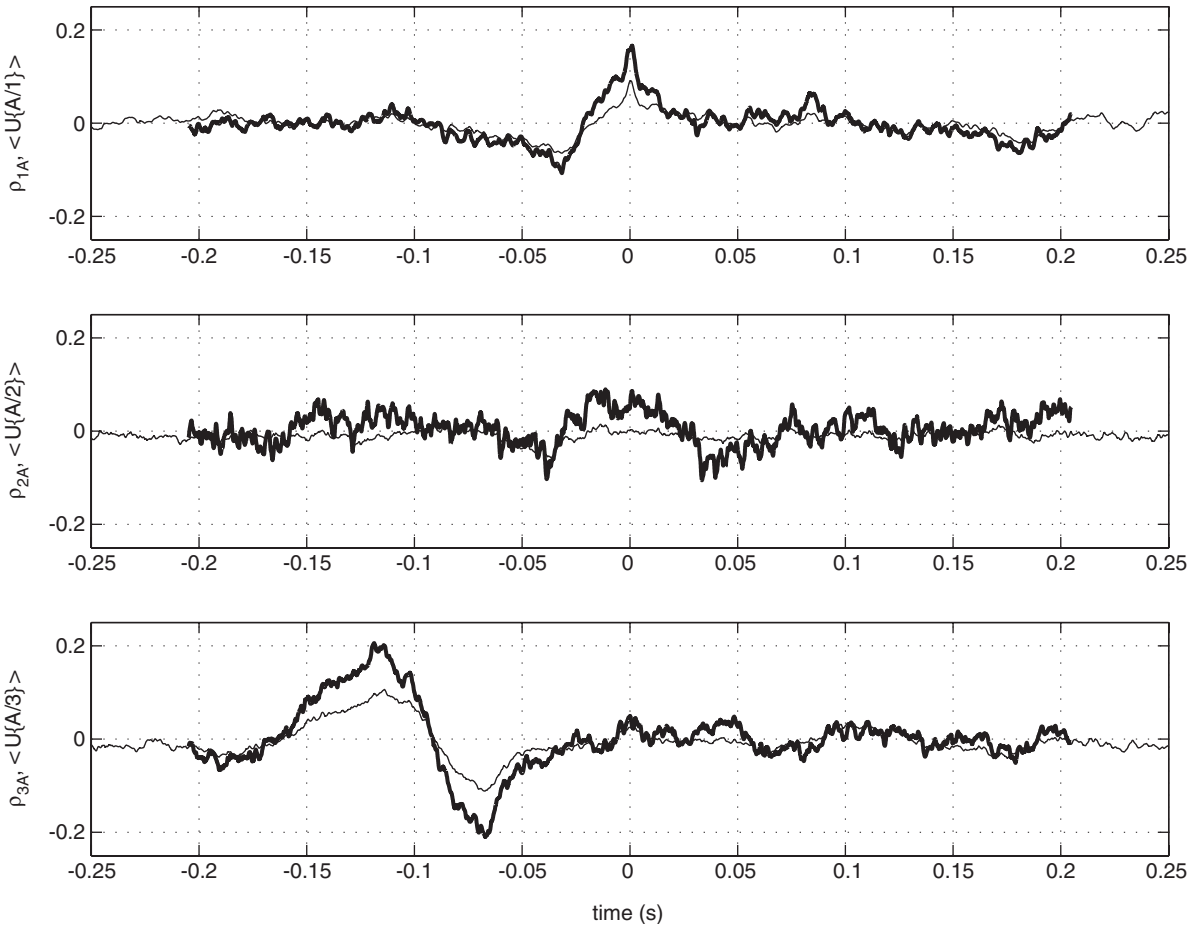

Fig. 17. Wall pressure peaks conditioned velocity structures (solid bold lines) and cross correlations (solid lines) between the anemometer A and wall microphones 1,2 and 3 (as reported in Fig. 8). The averaged velocity signatures are normalized with respect to the velocity standard deviation. Flow conditions are: $U = 10\,\mathrm{m/s}$, $H = 15\,\mathrm{mm}$, $L = 640\,\mathrm{mm}$ and $\delta = 25\,\mathrm{mm}$.

averaged signature with close-to-zero time delay, given the acoustic proximity of the two probes. This means that pressure peaks at the wall and flow structures passing the anemometer are almost simultaneous and are associated to the flow structures impacting onto the cavity wall in the vicinity of the first reattachment position x_R. It is finally pointed out that the plots of Fig. 17 display a marked similarity between the averaged velocity signatures obtained from the cross-conditioning method and those obtained from the cross-correlation coefficients, thus substantiating the achieved results.

In the region bounded by the first reattachment and the downstream step, the flow field is characterized by the passage of vortices convected past the cavity floor. Here, vortical structures convected downstream leave only partial traces on the probes located in the middle of the cavity. This is shown in Fig. 18 where cross-correlations involve the anemometer B located at the center of the cavity and non-zero averaged signatures are no longer observed.

4.2. Proposed scaling and universal form-functions

The results presented above clarified the main physical phenomena underlying the generation of the largest wall pressure fluctuations at the first reattachment point and in the vicinity of the downstream step. A relevant

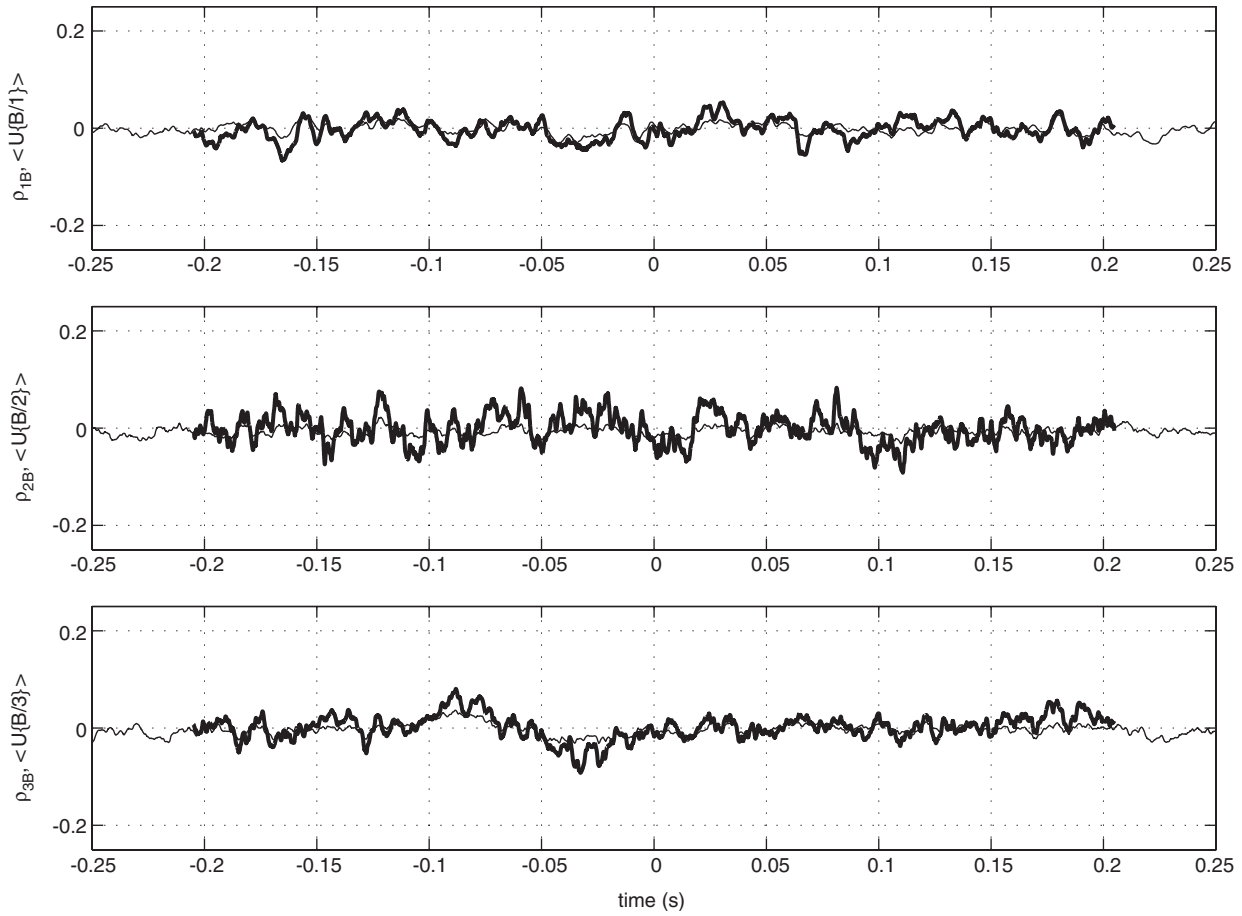

Fig. 18. Same as Fig. 17 but for the anemometer B. Results analogous to those of Hot Wire *B* are obtained for the Hot wire *C* and are not reported for brevity.

result is that the physical mechanism underlying the largest SPL seems not to change within the range of geometries and flow conditions considered in this study. An attempt to achieve a general representation of both the SPL and the PSD along the cavity can therefore be conducted.

Figs. 10 and 12 have shown that, in agreement with the analysis of Ref. [23], a satisfactory collapse of the PSD as well as of the SPL cannot be achieved by a simple non-dimensionalization of the dependent variables into G'_{pp} and SPL′.

A more complete scaling is here proposed basing on the hypothesis of separation of variables. The approach adopted is similar to the acoustic similarity laws developed for fans [43,44] and leading to general relationships among the non-dimensional parameters. The dimensionless spectrum G'_{pp} can be represented as a function of the dimensionless groups defined in Section 2, leading to the following expression:

$$G'_{pp}(St_H, x', \Delta, Re_H, \gamma, \Lambda) = G''_{pp}(St_H, x')\Delta^{\alpha_1} Re_H^{\alpha_2}\gamma^{\alpha_3}\Lambda^{\alpha_4}. \tag{6}$$

As for the SPL′ in Eq. (3), the analogous SPL″ can be defined. Therefore, integrating Eq. (6) and taking the logarithm, the following expression is obtained:

$$\mathrm{SPL}' = \alpha_1 10\log_{10}\Delta + \alpha_2 10\log_{10} Re_H + \alpha_3 10\log_{10}\gamma + \alpha_4 10\log_{10}\Lambda + \mathrm{SPL}''. \tag{7}$$

In our approximation, in order for a general model to be obtained, it is assumed that the shape of the spectra remains similar along the cavity while the overall dependence upon x' is retrieved by the variation of the SPL″

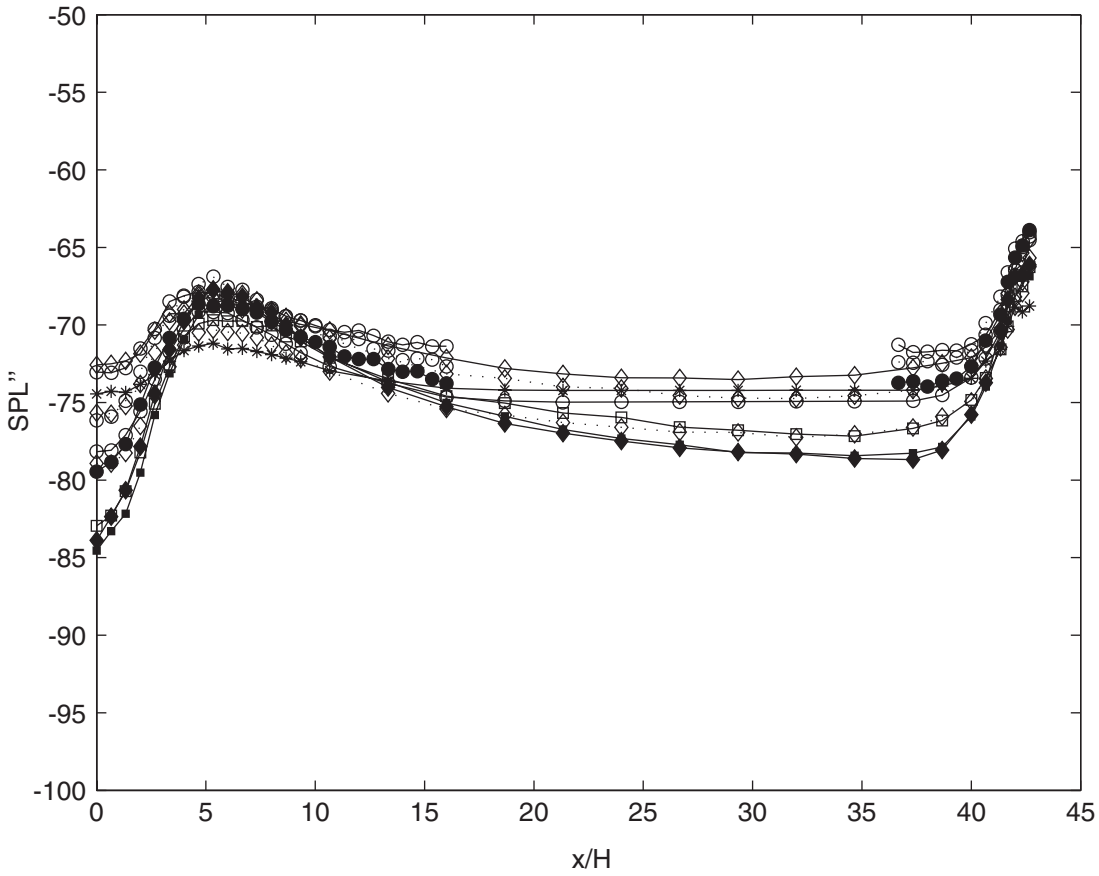

Fig. 19. SPL″ distribution along the cavity for different flow conditions. Symbols are the same as in Fig. 10. The y-scale range is the same as that of Fig. 8 in order to better appreciate the collapse of the normalized points.

which gives a modulation of the spectral energy, the same amount at the different frequencies. The set of optimal exponents $\alpha_i\,(i=1,\ldots,4)$ is found by minimizing the mean square error of SPL″ for the different tests presently analyzed and the following result is obtained:

$$\alpha_1=-1.2,\quad \alpha_2=-0.1,\quad \alpha_3=-3.3,\quad \alpha_4\simeq 0. \tag{8}$$

It is found, as expected, that the dependence upon $\Lambda=L/H$ can be neglected and a weak dependence upon Re_H is also documented. This result is in agreement with the experimental findings of Ref. [16], where a weak dependence upon Re_H even at supersonic flow conditions was found. Results obtained at $H=15\,\text{mm}$ and $U=30\,\text{m/s}$ were not used to determine Eq. (8), since they will be used as reference test cases in the validation procedure that is described later on. The SPL″ as functions of x' and at different inflow conditions are reported in Fig. 19. The collapse of the curves for the different flow conditions is reasonable mainly in correspondence of the regions where the largest pressure fluctuations are measured, that is at the first reattachment point and in the vicinity of the second step. In these regions the effect of background noise, is negligible and the signal to noise ratio is the highest.

The modulation effect of the dimensionless spectra amplitude retrieved by the SPL″ variation along x', can be expressed in terms of a universal form function $\Psi(x')$ which is obtained by averaging the experimental SPL″ over the whole test conditions. It is therefore possible to write:

$$G''_{pp}(St_H,x')=G'''_{pp}(St_H)\Psi(x'). \tag{9}$$

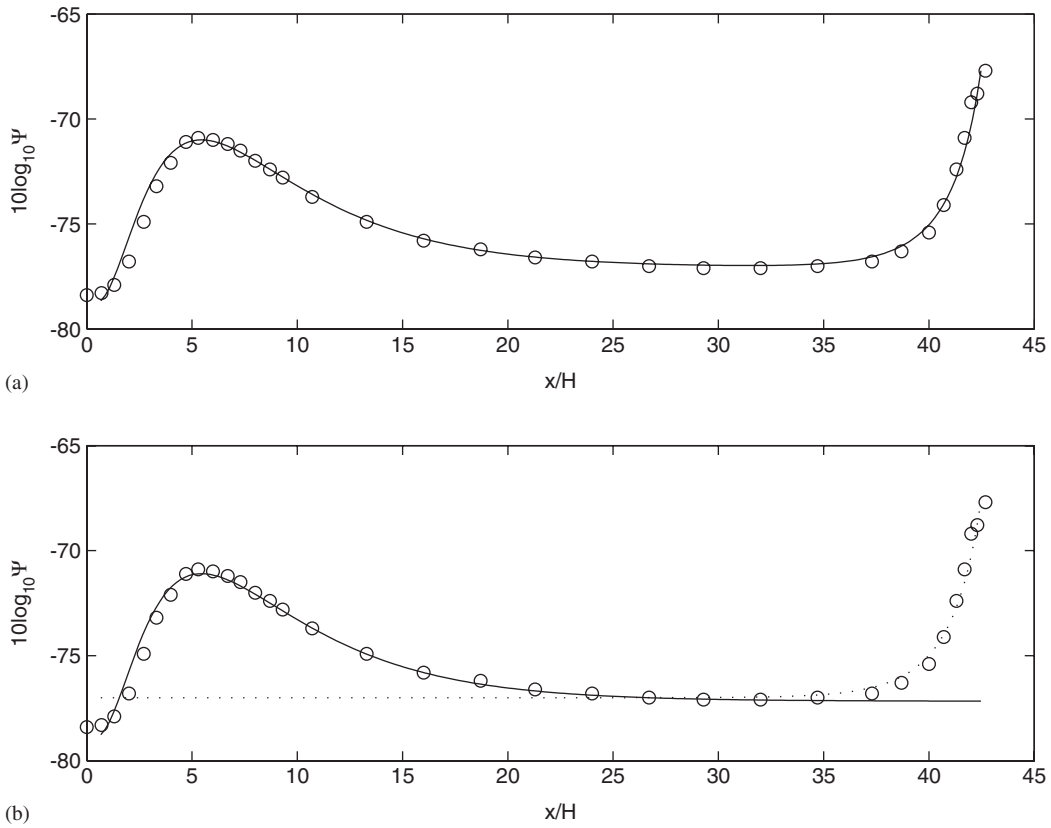

Fig. 20. Universal form function reproducing the averaged SPL″ along the cavity. (a) Solid line is the analytical approximation reported in Eq. (11) while symbols denote the experimental results. (b): the two contributions F_1 (solid line) and F_2 (dotted line) of Eq. (11) are reported separately.

The quantity G''''_{pp} denotes spectra with corresponding unitary SPL‴. The universal function $\Psi(x')$ is computed by assuming $\overline{\mathrm{SPL}}''' = 1$ and averaging over all the test conditions again excluding only results obtained at $H = 15\,\mathrm{mm}$ and $U = 30\,\mathrm{m/s}$. The analytical expression which leads to the $\Psi(x')$ function is the following:

$$\mathrm{SPL}''' = -10\log_{10}[\Psi(x')] + \langle \mathrm{SPL}'' \rangle = 1, \tag{10}$$

where the symbol $\langle \ldots \rangle$ denotes the ensemble averaging.

The achieved universal form-function is reported in Fig. 20 together with an analytical approximation which is given by the following universal dimensionless formula:

$$10\log_{10}[\Psi(x')] = F_1(x') + F_2(x') + C, \tag{11}$$

where

$$F_1(x') = -19\left[\operatorname{sech}\frac{x'}{2.1} - 0.93\tanh\frac{x'}{10}\right]$$

gives the behavior close to the first step reattachment,

$$F_2(x') = \frac{1}{1 - 0.38\exp[0.5(x' - \Lambda)]}$$

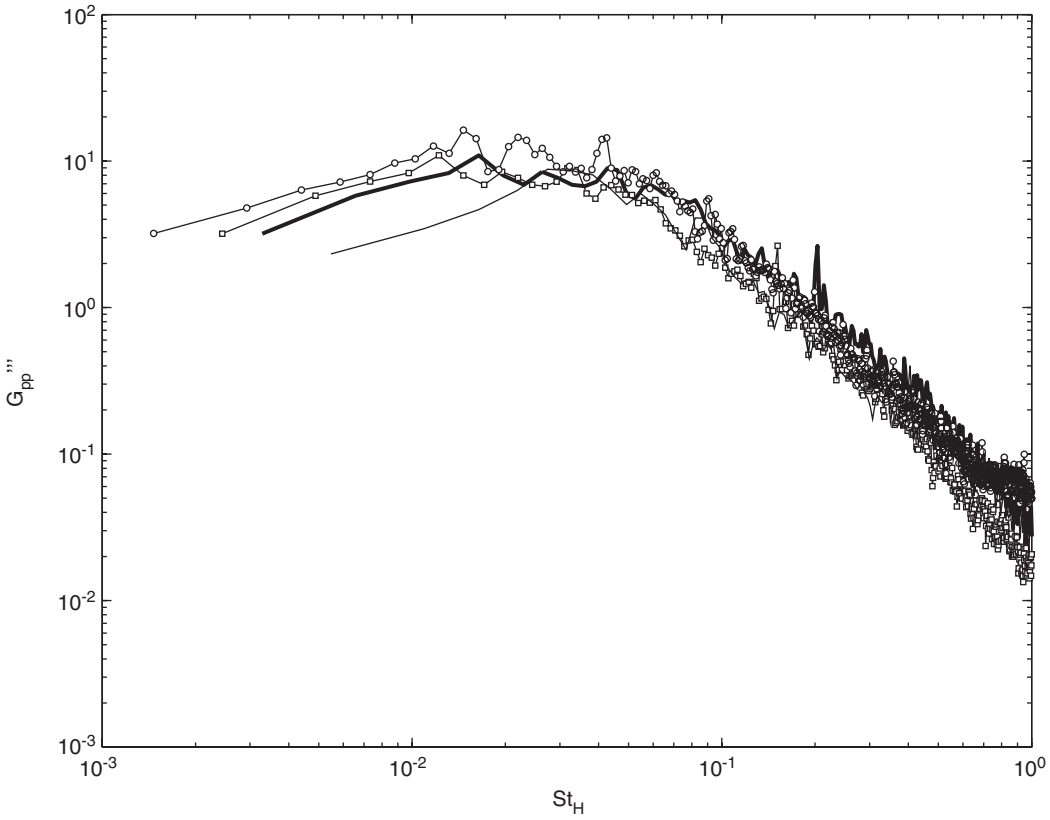

Fig. 21. Examples of G_{pp}''' computed at $x' = 7$ the following flow conditions: $U = 30\,\mathrm{m/s}$, $H = 15\,\mathrm{mm}$, $L = 640\,\mathrm{mm}$ (solid bold line with no symbols); $U = 50\,\mathrm{m/s}$, $H = 25\,\mathrm{mm}$, $L = 640\,\mathrm{mm}$ (solid line with '□' symbols); $U = 30\,\mathrm{m/s}$, $H = 15\,\mathrm{mm}$, $L = 640\,\mathrm{mm}$ (solid line with '○' symbols); $U = 50\,\mathrm{m/s}$, $H = 25\,\mathrm{mm}$, $L = 640\,\mathrm{mm}$ (solid line with no symbols).

reproduces the SPL increase close to the second step and

$$C = -78.4$$

is an offset.

Once the function $\Psi(x')$ is known, the normalized spectra $G_{pp}'''(St_H)$ can be obtained from Eq. (9). Examples obtained in the vicinity of the first reattachment point at different flow conditions are reported in Fig. 21, showing a good collapse. According to the results presented in Fig. 19, the collapse of the spectra in the central region of the cavity is not as satisfactory. As for the universal SPL, also in this case a universal spectrum can be obtained by averaging the experimental $G_{pp}'''(St_H)$. In this case, the average can be taken also along x', thus a number of about 400 spectra are averaged together giving an averaged spectrum that represents the non-dimensional PSD shape function. The final result is reported in Fig. 22 together with the analytical approximation (G_{pp}^a) that is obtained by a fourth order polynomial fit to the logarithmic data, that follows:

$$\log_{10}[G_{pp}^a] = 0.214[\log_{10} St_h]^4 + 1.04[\log_{10} St_h]^3 + 0.773[\log_{10} St_h]^2 - 1.978[\log_{10} St_h] - 1.247. \quad (12)$$

The model proposed therefore consists of the scaling exponents reported in Eq. (8) together with the universal form functions giving the analytical representation of SPL$''$ and of $G_{pp}'''(St_H)$. The model is tested by reproducing dimensional spectra and original SPL of some test cases which were not included into the modeling procedure. An example of SPL reproduction is reported in Fig. 23, where the reported error band

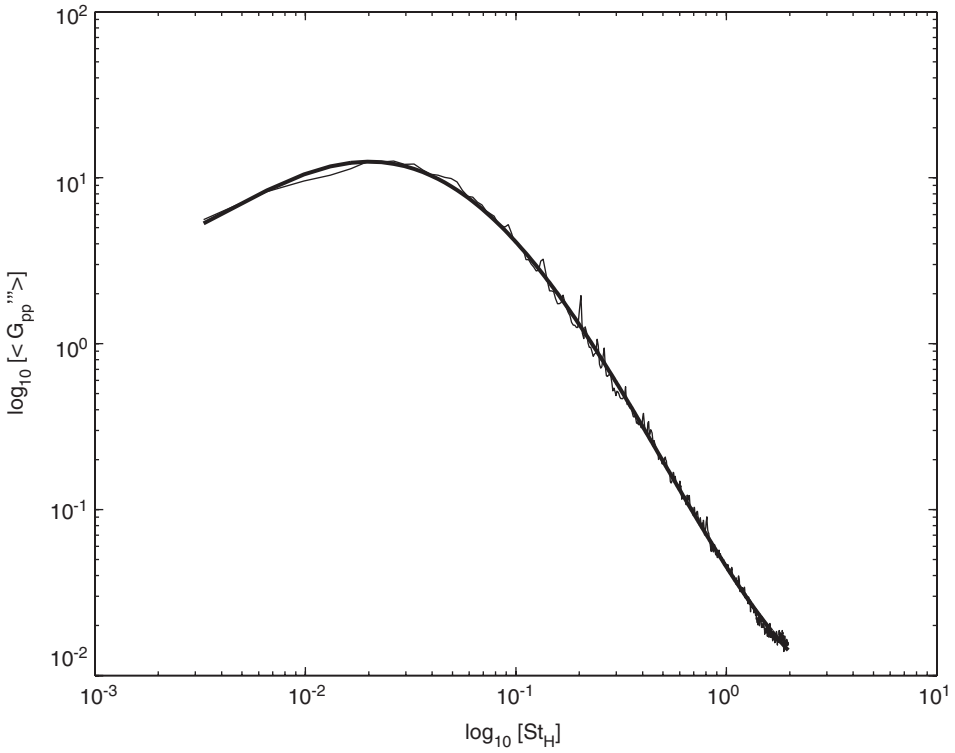

Fig. 22. Universal form spectrum reproducing the averaged G'''_{pp}. The solid line denotes the experimental results and the solid bold line is the analytical approximation reported in Eq. (12).

accounts for the data dispersion in the averaging procedure, leading to the universal form-functions. The capability of the model to reproduce the overall noise along the whole cavity seems reasonably good. Examples of dimensional PSD reproduction are reported in Figs. 24 and 25. As with the SPL results (Fig. 23), the agreement between measured and modeled quantities is satisfactory, especially in the vicinity of the regions where the largest pressure fluctuations occur, while larger deviations of up to 5 dB, are observed in intermediate regions.

5. Conclusions

An experimental characterization of the wall pressure fluctuations at low Mach numbers has been conducted in a large AR shallow cavity model made by a backward-facing step followed by a forward-facing step. In this shallow cavity, the steps separation distance is much larger than the steps height. Several measurements were performed with hot wire anemometers in the flow and with high resolution microphones at the wall at different flow conditions, to characterize the flow physics. Spectral data have been obtained by successfully applying a spectral method to reduce the background noise. A signal conditioning method based on the wavelet transform of the wall pressure time series has been applied to determine the most energetic pressure time signatures. Cross-correlations and cross-conditioning of velocity/pressure signals have also been performed to explore the fluid dynamic behavior and clarify basic physical mechanisms underlying the generation of the largest pressure fluctuations at the cavity wall.

The SPL distributions along the plate highlighted that the dimensionless reattachment point downstream the first backward-facing step is weakly influenced by the dimensionless parameters and it is always located at $\simeq 6H$ while the SPL maximum magnitude is reached in the vicinity of the downstream step.

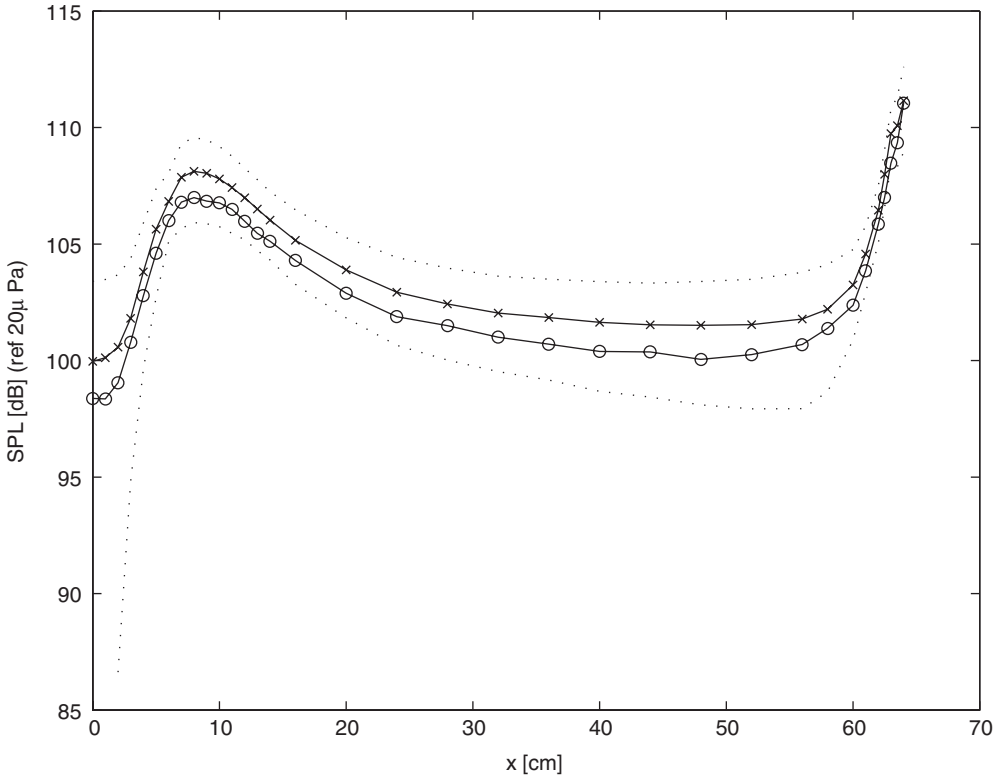

Fig. 23. Example of the reconstructed SPL (∗) compared to the measured one (○). Dashed lines delimit the error band of the modeled SPL, and defined as one standard deviation from the averaged SPL″. The case considered corresponds to: $U = 30\,\mathrm{m/s}$, $H = 15\,\mathrm{mm}$, $L = 640\,\mathrm{mm}$ and $\delta = 25\,\mathrm{mm}$. This case was not included in the modeling procedure.

The spatial evolution of the most energetic averaged pressure time signatures as well as the velocity/pressure cross-conditioned structures have evidenced that the aerodynamic pressure fluctuations in the vicinity of the upstream step are due to the reattachment phenomenon while at the downstream step the largest pressure fluctuations at the wall are associated with the vortical structures impacting the vertical side. From the practical viewpoint this result implies that an aerodynamic control at the upstream step would be effective in the overall SPL abatement also in correspondence of the downstream step.

The experimental results confirm that a separation of variables approach is appropriate to determine the dependence of the most relevant spectral quantities upon the governing parameters. Both the wall pressure spectra and SPL distributions along the cavity displayed a satisfactory data collapse, when properly normalized and parameterized. The quality of this data reduction was best within the regions not too close to the two steps, where flow recirculation occurs. The spectra dependence upon the dimensionless parameters is determined by power laws, yielding to a linear dependence in terms of SPL, and an optimization procedure was applied to retrieve the best scaling exponents, based on the minimization of the data dispersion with respect to the mean. It was found that the parameter $\Lambda = L/H$ can be neglected, while the exponent of the Re_H number is very small and thus this parameter plays a weak role.

Empirical formulae representing the dimensionless SPL and dimensionless frequency spectra have been proposed. The ability of the model to correctly approximate the actual shape of the spectral quantities has been tested by reproducing dimensional SPL and spectra obtained in the present experiment. The results obtained seem satisfactory and encouraging but the proposed model should be further tuned and assessed by considering data from other experiments and by a direct comparison with in-flight data.

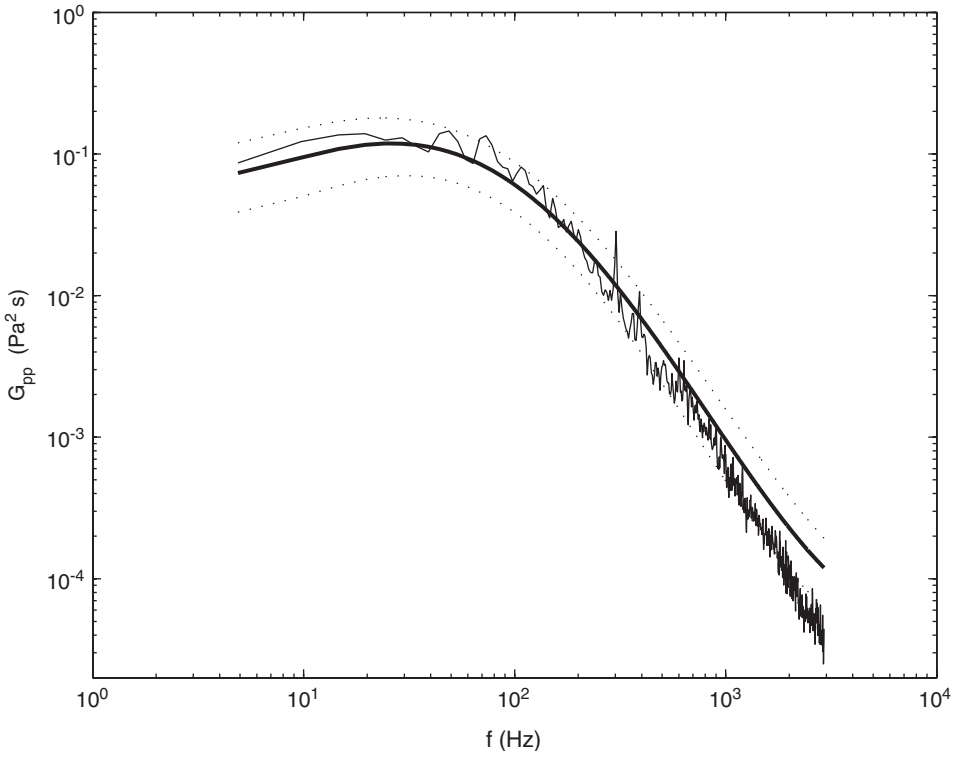

Fig. 24. Example of the reconstructed dimensional spectrum (solid bold line) compared to the measured one (solid). Dashed lines denote the error-bars of the modeled spectrum obtained from the standard deviation of the averaged G'''_{pp}. The case considered corresponds to: $U = 30\,\mathrm{m/s}$, $H = 15\,\mathrm{mm}$, $L = 640\,\mathrm{mm}$, and axial position $x' = 6$ and was not included in the modeling procedure.

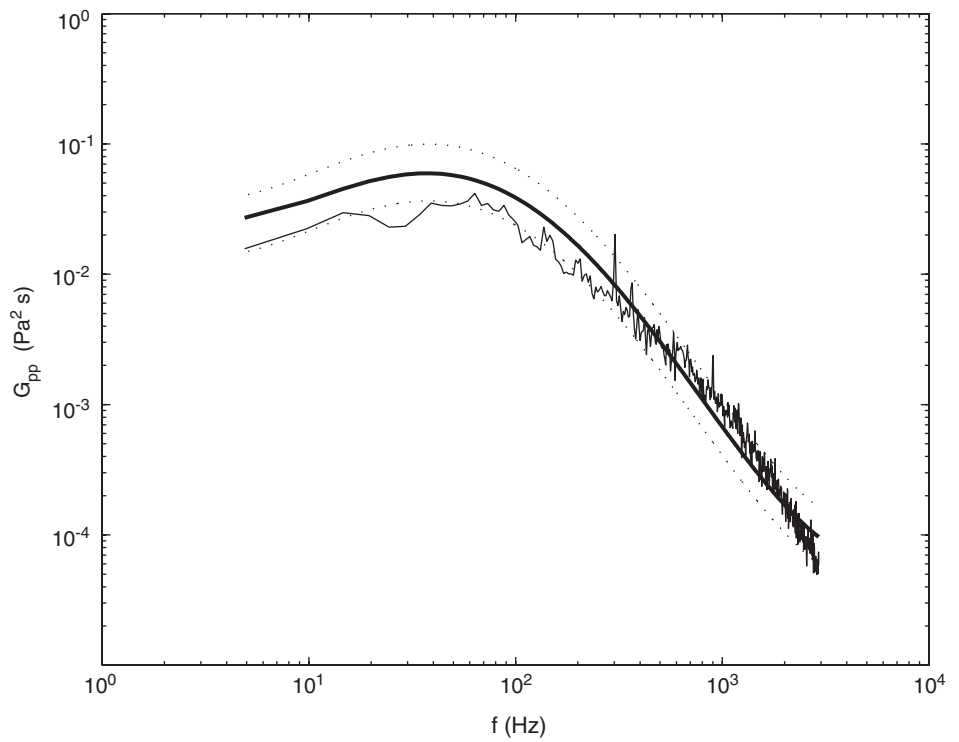

Fig. 25. Same as Fig. 24 but for the axial position $x' = 20$.

Acknowledgements

The authors wish to sincerely thank A. Rona for his extensive comments on the draft paper and his suggestions for data interpretation. S. Neroni and M. Croella are sincerely acknowledged for helping us during measurements and data analysis. D. Prischitch of ENEA is acknowledged for his support during the experimentation at the ENEA wind tunnel. This work has been developed under a EU grant GRD1-1999-10487 within the 5th Framework Programme.

References

[1] W.K. Blake, Mechanics of flow induced sound and vibrations, *Applied Mathematics and Mechanics*, Academic Press, Orlando, FL, 1986.
[2] M.K. Bull, Wall pressure fluctuations beneath turbulent layer: some reflections on forty years of research, *Journal of Sound and Vibration* 190 (1996) 299–315.
[3] Y. Na, P. Moin, The structure of wall-pressure fluctuations in turbulent boundary layers with adverse pressure gradient and separation, *Journal of Fluid Mechanics* 377 (1998) 347–373.
[4] H.H. Hubbard, Some experiments related to the noise from boundary layers, *Journal of the Acoustical Society of America* 29 (1957) 331–334.
[5] H.H. Hubbard, *Aeroacoustics of Flight Vehicles: Theory and Practice*, Vol. 1, Noise Sources, Nasa Reference Publisher 1258, Woodbury, NY, Published by A.I.P, 1995.
[6] F.R. Fricke, D.C. Stevenson, Pressure fluctuations in a separated flow region, *Journal of the Acoustical Society of America* 44 (1968) 1189–1200.
[7] L.M. Hudy, A.M. Naguib, W.M. Humphreys, Jr., S.M. Bartram, Wall-pressure-array measurements beneath a separating/reattaching flow region, AIAA Paper 2002, 2002–0579.
[8] C. Noger, J.C. Patrat, J. Peube, J.L. Peube, Aeroacoustical study of the TGV pantograph recess, *Journal of Sound and Vibration* 231 (2000) 563–575.
[9] S. Grace, An overview of computational aeroacoustic techniques applied to cavity noise prediction, AIAA Paper 2001-0510, 2001.
[10] D. Rockwell, E. Naudascher, Review of self-sustaining oscillations of flow past cavities, *Journal of Fluids Engineering* 100 (1998) 152–165.
[11] V. Brederode, P. Bradshaw, Influence of the side walls on the turbulent center-plane boundary-layer in a square duct, *Journal of Fluids Engineering* 100 (1978) 91–96.
[12] R.L. Simpson, Turbulent boundary-layer separation, *Annual Review of Fluid Mechanics* 21 (1989) 205–234.
[13] H. Le, P. Moin, J. Kim, Direct numerical simulation of turbulent flow over a backward-facing step, *Journal of Fluid Mechanics* 330 (1997) 349–374.
[14] I. Lee, H.J. Sung, Multiple-arrayed pressure measurement for investigation of the unsteady flow structure of a reattaching shear layer, *Journal of Fluid Mechanics* 463 (2002) 377–402.
[15] B.M. Efimtsov, N.M. Kozlov, S.V. Kravchenko, A.O. Andersson, Wall pressure-fluctuation spectra at small backward-facing steps, AIAA Paper 2000–2053, 2000.
[16] B.M. Efimtsov, N.M. Kozlov, S.V. Kravchenko, A.O. Andersson, Wall pressure-fluctuation spectra at small forward-facing steps, AIAA Paper 1999–1964, 1999.
[17] D.J.J. Leclercq, M.C. Jacob, A. Louisot, C. Talotte, Forward-backward facing step pair: aerodynamic flow, wall pressure and acoustic characterisation, AIAA Paper 2001–2249, 2001.
[18] D.G. Mabey, Analysis and correlation of data on pressure fluctuations in separated flow, *Journal of Aircraft* 9 (1972) 642–645.
[19] A. Kiya, K. Sasaki, M. Arie, Discrete-vortex simulation of a turbulent separation bubble, *Journal of Fluid Mechanics* 120 (1982) 219–244.
[20] T.M. Farabee, An experimental investigation of wall pressure fluctuations beneath non-equilibrium turbulent flow, Ph.D. Thesis, Catholic University of America, 1986.
[21] J. Ffowcs Williams, Noise source mechanisms, in: D.G. Crighton, A.P. Dowling, J.E. Ffowcs Williams, M.A. Heckl, F.A. Leppington (Eds.), *Modern Methods in Analytical Acoustics: Lecture Notes*, 1992, pp. 313–354
[22] J.S. Bendat, A.G. Piersol, *Random Data: Analysis and Measurements Procedures*, third ed., Wiley, New York, 2000.
[23] T.A. Brungart, G.C. Lauchle, S. Deutsch, E.T. Riggs, Wall pressure fluctuations induced by separated/reattached channel flow, *Journal of Sound and Vibration* 251 (2002) 558–577.
[24] R. Camussi, G. Guj, D. Barbagallo, D. Prischich, Experimental characterization of the aeroacoustic behavior of a low speed wind tunnel, AIAA Paper 2000–1986, 2000.
[25] P. Bradshaw, Wind tunnel screens: flow instability and its effect on airfoil boundary layers, *Journal of the Royal Aeronautical Society* 68 (1964) 198–201.
[26] E.M. Laws, J.L. Livesey, Flows through screens, *Annual Review of Fluid Mechanics* 10 (1978) 247–266.
[27] H. Schlichting, *Boundary-Layer Theory*, McGraw-Hill, New York, 1986.
[28] M. Carley, J.A. Fitzpatrick, Spectral conditioning of propeller noise from broadband sources, *Journal of Sound and Vibration* 238 (2000) 31–49.

[29] R. Camussi, G. Guj, Orthonormal wavelet decomposition of turbulent flows: intermittency and coherent structures, *Journal of Fluid Mechanics* 348 (1997) 177–199.
[30] G. Guj, R. Camussi, Statistical analysis of local turbulent energy fluctuations, *Journal of Fluid Mechanics* 382 (1999) 1–26.
[31] C. Meneveau, Analysis of turbulence in the orthonormal wavelet representation, *Journal of Fluid Mechanics* 232 (1991) 469–520.
[32] S. Mallat, A theory for multiresolution signal decomposition: the wavelet representation, *IEEE Transaction PAMI* 11 (1989) 674–693.
[33] M. Farge, Wavelet transforms and their applications to turbulence, *Annual Review of Fluid Mechanics* 24 (1992) 395–457.
[34] G. Guj, M. Carley, R. Camussi, A. Ragni, Acoustic identification of coherent structures in a turbulent jet, *Journal of Sound and Vibration* 259 (2003) 1037–1065.
[35] G.C. Lauchle, W.A. Kargus, Scaling of turbulent wall pressure fluctuations downstream of a rearward facing step, *Journal of the Acoustical Society of America* 107 (2000) L1–L6.
[36] J.K. Eaton, J.P. Johnston, A review of research on subsonic turbulent flow reattachment, *AIAA Journal* 19 (1981) 1093–1100.
[37] D.M. Driver, H.L. Seegmiller, J.G. Marvin, Time-dependent behavior of a reattaching shear layer, *AIAA Journal* 25 (1987) 914–919.
[38] T.M. Farabee, M.J. Casarella, Measurements of fluctuating wall pressure for separated/reattached boundary layer flows, *Journal of Vibration, Acoustics, Stress and Reliability in Design* 108 (1986) 301–307.
[39] I. Lee, H.J. Sung, Characteristics of wall pressure fluctuations in separated and reattaching flows over a backward-facing step: Part I. Time-mean statistics and cross-spectral analyses, *Experiments in Fluids* 30 (2001) 262–272.
[40] N. Curle, The influence of solid boundaries upon aerodynamic sound, *Proceedings of the Royal Society of London A* 231 (1955) 505–514.
[41] A. Rona, Aerodynamics and aeroacoustics of oscillatory flows, Ph.D. Thesis, University of Southampton, 1997.
[42] J. Lighthill, On sound generated aerodynamically: I General theory, *Proceedings of the Royal Society of London A* 211 (1952) 564–587.
[43] J. Weidemann, Analysis of the relations between acoustic and aerodynamic parameters for a series of dimensionally similar centrifugal fan rotors, NASA-TT-F-13798 (DLR-FB-71-12), 1971, 798–801.
[44] W. Neise, B. Barsikow, Acoustic similarity laws for fans, *Journal of Engineering for Industry* 104 (1982) 162–168.